

# Compressive Sensing with Low Precision Data Representation: Theory and Applications

Nezihe Merve Gürel<sup>†</sup> Kaan Kara<sup>†</sup> Alen Stojanov<sup>†</sup> Tyler Smith<sup>†</sup> Dan Alistarh<sup>‡</sup>  
Markus Püschel<sup>†</sup> Ce Zhang<sup>†</sup>

<sup>†</sup>Department of Computer Science, ETH Zurich  
<sup>‡</sup>Institute of Science and Technology, IST Austria

## Abstract

Modern scientific instruments produce vast amounts of data, which can overwhelm the processing ability of computer systems. Lossy compression of data is an intriguing solution, but comes with its own dangers, such as potential signal loss, and the need for careful parameter optimization. In this work, we focus on a setting where this problem is especially acute—compressive sensing frameworks for radio astronomy—and ask: Can the precision of the data representation be lowered for *all* inputs, with both recovery guarantees and practical performance?

Our first contribution is a theoretical analysis of the Iterative Hard Thresholding (IHT) algorithm when all input data, that is, the measurement matrix and the observation, are quantized aggressively to as little as 2 bits per value. Under reasonable constraints, we show that there exists a variant of low precision IHT that can still provide recovery guarantees. The second contribution is an analysis of our general quantized framework tailored to radio astronomy, showing that its conditions are satisfied in this case. We evaluate our approach using CPU and FPGA implementations, and show that it can achieve up to  $9.19\times$  speed up with negligible loss of recovery quality, on real telescope data.

## 1. Introduction

The ability to collect, store, and process large amounts of data is enabling the next generation of *data intensive* scientific instruments. For example, the Square Kilometre Array (SKA), the largest radio telescope ever built, has thousands of dishes, and is expected to achieve a raw data throughput of 62 Exabytes by mid-2020. Such instruments require extremely advanced capabilities in terms of engineering, algorithms, calibration, and storage [25].

In this paper, we focus on compressive sensing [19, 14, 15], a popular mathematical framework behind some of these instruments, and aim to understand the impact of *representing all input data in lower precision, instead of 32-bit floating-point values*. We make the following contributions:

1. We develop a theoretical framework, which shows for the first time that, under technical conditions, Iterative Hard Thresholding (IHT), a popular algorithm for compressive sensing, converges with guarantees on the recovery quality when all input data is in lower precision.
2. We refine our results in the context of a real-world radio astronomy application and develop *stronger* application-specific guarantees for sky recovery by leveraging the properties of the measurement matrix in this scenario.

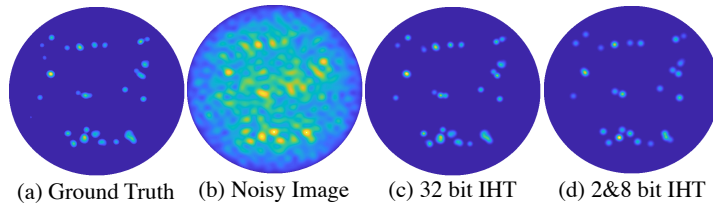


FIG 1. Illustration of the main results of this paper. Representing all input data at low precision, IHT achieves a negligible loss of recovery quality (data from LOFAR station CS302, 2 bit measurement matrix and 8 bit observation). We provide both analysis and the system implementation.

**3.** We implement and evaluate our approach on CPU and FPGA-based implementations, which achieve up to  $4.18\times$  and  $9.19\times$  speed-up to full recovery, respectively, on problems with a quantized dense measurement matrix. We believe the tools we developed can further generalize to other sparse reconstruction problems demanding high processing capability.

**Problem Formulation.** Compressive sensing (CS) [19, 14, 15] is a technique in sparse signal reconstruction that offers a range of efficient algorithms acquiring high dimensional signals from inaccurate and incomplete samples with an underlying sparse structure. Many real-life problems, e.g, medical imaging, interferometry, and genomic data analysis, can benefit from these techniques.

In mathematical terms, compressive sensing is formulated as follows. Let a sparse or approximately sparse signal  $\mathbf{x} \in \mathbb{R}^N$  be sampled via a linear sampling operator  $\Phi^{M \times N}$ . In matrix notation, the vector of measurements  $\mathbf{y} \in \mathbb{C}^M$  is

$$\mathbf{y} = \Phi \mathbf{x} + \mathbf{e}, \quad (1)$$

where  $\mathbf{e}$  is the observation noise and  $M < N$ .

CS recovery algorithms iteratively build up a sparse estimate  $\mathbf{x}$  such that  $\Phi \mathbf{x}$  approximates  $\mathbf{y}$  well, that is,  $\|\mathbf{y} - \Phi \mathbf{x}\|_2$  is small. The sparsity constraint imposed on  $\mathbf{x}$  overcomes this ill-posed problem, yet is computationally NP-hard due to its combinatorial nature. Therefore, most CS algorithms resort to convex relaxation of  $\ell_0$ -based optimization, or a collection of thresholding and greedy methods such as Iterative Hard Thresholding (IHT) [8, 9] and Compressive Sampling Matching Pursuit (CoSaMP) [33]. These and other methods, e.g. [32, 46, 47, 7, 33] face several challenges when applied to real-life problems: for provable guarantees, it is often required that (1) the measurement matrix  $\Phi$  satisfies the Restricted Isometry Property (RIP) [13, 17], and that (2) the sparsity level is chosen appropriately. Normalized IHT (NIHT) [10] releases the RIP condition by introducing a step size parameter, enabling rigorous guarantees for a broader class of practical problems. This paper builds upon this line of work.

We consider the sparse signal recovery problem in Eqn.(1) described as: given  $\mathbf{y}$  and  $\Phi$ , find coefficients  $\mathbf{x}$  minimizing the cost function

$$\|\mathbf{y} - \Phi \mathbf{x}\|_2^2 \quad \text{subject to } \|\mathbf{x}\|_0 \leq s, \quad \text{where } \|\mathbf{x}\|_0 = |\text{supp}(\mathbf{x})| = |\{i : x_i \neq 0\}|. \quad (2)$$

Under certain constraints, normalized IHT is guaranteed to approximate  $\mathbf{x}$  with high accuracy. Here, we consider the properties of this algorithm in a lossy compression setting,

	Assumption on $\Phi$	$Q(\Phi)$	$Q(y)$
Boufounos et al.	Gaussian	×	✓
Ai et al.	unit variance	×	✓
Jacques et al.	RIP	×	✓
Laska et al.	Gaussian & RIP	×	✓
Plan et al. (2011)	Gaussian & RIP	×	✓
Plan et al. (2012)	Gaussian	×	✓
Gupta et al.	Gaussian	×	✓
Gopi et al.	sub-Gaussian/binary & RIP	✓	✓
<b>This Paper</b>	non-symmetric RIP	✓	✓

FIG 2. Comparison of this paper with previous work.  $Q(\Phi)$  and  $Q(y)$  denote whether the paper considers quantizing  $\Phi$  and  $y$  (✓: yes).

where the data  $\mathbf{y}$  and  $\Phi$  consisting of floating-point values undergo a quantization process to a small set of discrete levels, a transformation denoted by  $Q$ . The goal of  $Q$  is to reduce the high cost of data transmission between the sensor or storage and the computational device (CPU, GPU, or FPGA). That is, we wish to recover  $\mathbf{x}$  using the modified NIHT update rule:

$$\mathbf{x}^{[n+1]} = H_s(\mathbf{x}^{[n]} + \mu^{[n]}Q(\Phi^\dagger)(Q(\mathbf{y}) - Q(\Phi)\mathbf{x}^{[n]})) \quad (3)$$

where  $H_s(\mathbf{x}) : \mathbb{C}^N \rightarrow \mathbb{C}^N$  the operator preserving only the largest  $s$  entries of  $\mathbf{x}$  in magnitude.

**Related work.** A series of previous studies made attempts to apply low precision to compressive sensing problems, summarized in Fig. 2. [12] demonstrates that sparse signals can be recovered with a scale factor when measurements preserve only sign information. [1, 18] show that approximately sparse signals can be robustly recovered from single-bit measurements sampled with a sub-Gaussian distribution. [27, 29] study a similar setting with a Gaussian measurement matrix, the so called Binary IHT [34, 35] and propose a computationally tractable and optimal recovery of 1-bit compressive sensing problem. [22, 21] give theoretical guarantees to recover the support of high dimensional sparse signals from 1-bit measurements.

This paper differs from prior work in two main ways: First, as we discuss in Section 3, our assumption that the measurement matrix being non-symmetric RIP is critical in radio astronomy applications, and none of these assumptions made by previous work would fit this use case. Second, we are the only work, with the exception of [21], that quantizes *both* the measurement matrix  $\Phi$  and the observations. [21] considers the problem of building a binary measurement matrix which can provide good support recovery guarantees given only one-bit measurements; by contrast, we consider a practical setting where we must quantize a given full-precision measurement matrix as well as possible, and can trade off higher precision for better recovery guarantees.

Another emerging line of work has been on low precision training for machine learning applications beyond compressive sensing. Examples include [37, 3, 48], and a series of works about partial or end-to-end low-precision training of deep networks [38, 26, 36, 50, 49, 31, 23]. These works focus on stochastic gradient descent (SGD); while IHT and related methods can be seen as a projected gradient methods, existing results, e.g. [48] focuses on the variance

added by quantization, and do not apply to recovery properties in the sparse case, which is the focus of this paper.

There has been significant research on designing efficient algorithms for sparse recovery [6, 43, 5, 16, 32]. We focus here on normalized IHT, and leave extensions to other methods as future work. We further note the work on recovery using sparse binary matrices, see e.g. [20] for a survey. The resulting matrix constructions could be applied in some cases, as they are pre-quantized, with similar guarantees. However, in applications such as the radio astronomy setting we consider, the measurement matrix is fixed and highly dense, in which case separate quantization is necessary.

## 2. Preliminaries

*Notation:* Scalars are denoted by italics, vectors by bold lower-case and matrices by bold upper-case. For all  $\mathbf{x} = (x_1, \dots, x_N) \in \mathbb{R}^N$ , we denote by  $\|\mathbf{x}\|_p$  the standard operator norm. Let  $\Phi \in \mathbb{C}^{M \times N}$ , let  $\Phi_{m,n} \in \mathbb{C}$  denote the matrix element in the  $m$ 'th row and  $n$ 'th column, and denote by  $\Phi_\Gamma$ . Finally  $32 \text{ bit}$  denotes the full precision scheme and  $b_\Phi$  &  $b_y$  bit precision denote the number of bits used to represent the measurement matrix  $\Phi$  and vector of observations  $\mathbf{y} \in \mathbb{C}^M$ , respectively.

In this section, we review existing results on the normalized IHT (NIHT) algorithm [10, 11]. Our results can be generalized to IHT if the measurement matrix satisfies  $\|\Phi\|_2 < 1$ . NIHT however alleviates this constraint by counteracting the scaling of  $\Phi$  with an adaptive step size  $\mu$  such that  $\|\mu^{0.5}\hat{\Phi}\|_2^2 < 1$  to ensure the convergence.

**Iterative Hard Thresholding.** Let  $\mathbf{x}^{[0]} = 0$ . NIHT has the following update rule:

$$\mathbf{x}^{[n+1]} = H_s(\mathbf{x}^{[n]} + \mu^{[n]}\Phi^\dagger(\mathbf{y} - \Phi\mathbf{x}^{[n]})), \quad (4)$$

where  $\mu^{[n]} > 0$  is the adaptive step size parameter, and  $H_s(\mathbf{x})$  is the thresholding operator that preserves the largest  $s$  (in magnitude) entries.

**Convergence.** The analysis of hard thresholding algorithms relies on the scaling properties of  $\Phi$ . Concretely, one must often deal with the non-symmetric Restricted Isometry Property (RIP) condition: a matrix  $\Phi$  satisfies non-symmetric RIP if

$$\alpha_s \leq \frac{\|\Phi\mathbf{x}\|_2}{\|\mathbf{x}\|_2} \leq \beta_s \quad (5)$$

for all  $\mathbf{x} : \|\mathbf{x}\|_0 \leq s$ , and where  $0 < \alpha_s, \beta_s \in \mathbb{R}$ ,  $\alpha_s \leq \beta_s$ , the so-called Restricted Isometric Constants (RICs). Remark that, for any support set  $\Gamma$  such that  $|\Gamma| \leq s$ ,  $\alpha_s$  and  $\beta_s$  are lower and upper bounded by the smallest and largest singular values of  $\Phi_{|\Gamma|}$ , respectively.

**Remark 1.** *The convergence of NIHT depends conditionally on the step size parameter  $\mu^{[n]}$ , unlike the traditional IHT approach where  $\mu^{[n]} = 1$ . While the traditional approach requires a re-scaling of the measurement matrix such that  $\|\Phi\|_2 < 1$  to ensure convergence, introducing a step size parameter enables the arbitrary scaling of  $\Phi$  hence relaxing the bounds on its norm. The role of  $\mu^{[n]}$  here is to compensate for this re-scaling by accordingly avoiding the undesirable amplification of noise, i.e., the ratio  $\|\Phi\mathbf{x}\|_2/\|\mathbf{e}\|_2$  remains unchanged.*

The main convergence result of NIHT can be stated as follows.

**Theorem 1.** [11] *Let  $\Phi$  be full rank, and  $s \leq m$ . If  $\beta_{2s} \leq \mu^{-1}$ , then NIHT converges to a local minimum of Eqn.(2).*

**Step Size Determination.** When setting the step size parameter, the condition  $\beta_{2s} \leq \mu^{-1}$ , which ensures convergence, poses the challenge that, to date, there is no efficient strategy to determine the exact values of RICs  $\beta_s$  and  $\alpha_s$  for an arbitrary measurement matrix in a computationally efficient manner. However, these constants can be bounded efficiently, and it can however be shown that randomly constructed measurement matrices can satisfy the RIP with high probability [13, 17]. We now briefly review strategies for setting the step size.

If the support of  $\mathbf{x}^{[n]}$  is preserved between iterations, we can set the step size adaptively [10] to

$$\mu^{[n]} = \frac{\mathbf{g}_{\Gamma^{[n]}}^T \mathbf{g}_{\Gamma^{[n]}}}{\mathbf{g}_{\Gamma^{[n]}}^T \Phi_{\Gamma^{[n]}}^T \Phi_{\Gamma^{[n]}} \mathbf{g}_{\Gamma^{[n]}}}, \quad (6)$$

where  $\mathbf{g}^{[n]} = \Phi^T(\mathbf{y} - \Phi \mathbf{x}^{[n]})$ . Clearly, the maximal reduction in cost function can then be attained. However, if the support of  $\mathbf{x}^{[n+1]}$  differs from that of  $\mathbf{x}^{[n]}$ , the sufficient convergence condition becomes

$$\mu^{[n]} \leq (1 - c) \frac{\|\mathbf{x}^{[n+1]} - \mathbf{x}^{[n]}\|_2^2}{\|\Phi(\mathbf{x}^{[n+1]} - \mathbf{x}^{[n]})\|_2^2}, \text{ for any small constant } c. \quad (7)$$

If the above condition is not met, a new proposal for  $\mathbf{x}^{[n+1]}$  can be calculated by using  $\mu^{[n]} \leftarrow \mu^{[n]}/(k(1 - c))$ , where  $k$  is a shrinkage parameter such that  $k > 1/(1 - c)$ . This adaptive setting of step size parameter is shown to provide RIP-invariant convergence as follows.

**Theorem 2.** [10] *Consider a noisy observation  $\mathbf{y} = \Phi \mathbf{x} + \mathbf{e}$  with an arbitrary vector  $\mathbf{x}$ . If  $\text{rank}(\Phi) = m$  and  $\text{rank}(\Phi_{\Gamma}) = s \quad \forall \Gamma : |\Gamma| = s$ , then the normalized IHT algorithm converges to a local minimum of the cost function Eqn.(2). Also, assume  $\Phi$  is non-symmetric RIP $_{2s}$  and let  $\gamma_{2s} = \max(1 - \alpha_{2s}/\beta_{2s}, \beta_{2s}/\alpha_{2s} - 1)$ . If  $\gamma_{2s} \leq 1/8$ , then*

$$\|\mathbf{x} - \mathbf{x}^n\|_2 \leq 2^{-n} \|\mathbf{x}^s\|_2 + 8\epsilon_s \quad (8)$$

where

$$\epsilon_s = \|\mathbf{x} - \mathbf{x}^s\|_2 + \frac{\|\mathbf{x} - \mathbf{x}^s\|_1}{\sqrt{s}} + \frac{1}{\beta_{2s}} \|\mathbf{e}\|_2. \quad (9)$$

After at most  $n^* = \log_2(\|\mathbf{x}^s\|_2/\epsilon_s)$  iterations, the recovery error bound in Eqn.(8) can be further simplified to

$$\|\mathbf{x} - \mathbf{x}^n\|_2 \leq 9\epsilon_s. \quad (10)$$

The above result suggests that, after a sufficiently large number of iterations, the reconstruction error is induced only by the noise  $\mathbf{e}$  and that  $\mathbf{x}$  is not exactly  $s$ -sparse.

### 3. Low Precision Iterative Thresholding

We now analyze a quantized version of IHT in terms of signal recovery performance. The key development here is that, by reducing the bit widths of the data points in a structured

manner, we can upper bound the recovery error. In Section 4, we will show that for one specific application, in radio astronomy we expect this error to be small, due to the structure of the measurement matrix.

As introduced earlier, let  $\mathbf{x}^{[0]} = 0$  and use the iteration

$$\mathbf{x}^{[n+1]} = H_s(\mathbf{x}^{[n]} + \hat{\mu}^{[n]} Q_b(\hat{\Phi}^\dagger)(Q_b(\mathbf{y}) - Q_b(\hat{\Phi})\mathbf{x}^{[n]})), \quad (11)$$

where  $Q(\cdot)$  is the quantization function that maps single-precision floating-point values onto a co-domain where each element has  $b$ -bits precision.

**Quantization.** We analyze a stochastic quantization function denoted with  $Q_b(\mathbf{v})$ , where  $\mathbf{v} = (v_1, v_2, \dots, v_d) \in \mathbb{R}^d$  is an arbitrary vector and  $b$  is the total number of bits used to represent it.  $\mathbf{v}$  can then be quantized into  $\ell = 2^b$  levels as follows. Let  $\ell_i, i \in \{1, 2, \dots, \ell - 1\}$  denote  $\ell$  equally spaced points on  $[-1, 1]$  such that  $\ell_1 = -1, \ell_\ell = +1$  and  $\ell_1 \leq \ell_2 \leq \dots \leq \ell_\ell$ , also  $v_j$  for  $j \in \{1, 2, \dots, d\}$  fall into the interval  $[\ell_i, \ell_{i+1}]$ . Stochastic quantization assigns the point to its nearest levels by setting

$$Q_b(v_j) = \begin{cases} \ell_i, & \text{with probability } \frac{\ell_{i+1} - v_j}{\ell_{i+1} - \ell_i} \\ \ell_{i+1}, & \text{otherwise.} \end{cases}$$

The quantization  $Q(\cdot)$  is unbiased, i.e.,  $\mathbb{E}[Q_b(\mathbf{v})] = \mathbf{v}$ . Let  $\hat{\Phi}$  represent the quantized matrix (or vector)  $\Phi$  and we drop the  $Q_b(\cdot)$  notation. Detailed steps are given in Algorithm 1.

**Convergence.** The modified algorithm attains a local minimum of the cost function  $\mathbb{E}[\|\hat{\mathbf{y}} - \hat{\Phi}\mathbf{x}\|_2^2]$  such that  $\|\mathbf{x}\|_0 \leq s$ . This can be majorized by the following surrogate objective function

$$\mathbb{E}[\|\mu^{0.5}\hat{\mathbf{y}} - \hat{\Phi}\mathbf{x}\|_2^2 + \|\mathbf{x} - \mathbf{x}^{[n]}\|_2^2 - \|\mu^{0.5}\hat{\Phi}(\mathbf{x} - \mathbf{x}^{[n]})\|_2^2],$$

whenever  $\|\mu^{0.5}\hat{\Phi}\|_2^2 < 1$ . If this condition is met, the minimizer of the above surrogate objective:  $\mathbf{x}^{[n+1]}$  ensures that  $\mathbb{E}[\|\hat{\mathbf{y}} - \hat{\Phi}\mathbf{x}^{[n+1]}\|_2^2] \leq \mathbb{E}[\|\hat{\mathbf{y}} - \hat{\Phi}\mathbf{x}^{[n]}\|_2^2]$ . Moreover, by using the arguments of [8], Eqn.(11) can be shown to minimize the expected cost  $\mathbb{E}[\|\hat{\mathbf{y}} - \hat{\Phi}\mathbf{x}\|_2^2]$ .

**Conditions on  $\hat{\Phi}$ .** The non-symmetric RIP holds for the quantized measurement matrix if

$$\hat{\alpha}_s \leq \frac{\|\hat{\Phi}\mathbf{x}\|_2}{\|\mathbf{x}\|_2} \leq \hat{\beta}_s, \forall \mathbf{x} : \|\mathbf{x}\|_0 \leq s. \quad (12)$$

Due to its non-symmetric nature, i.e.,  $\|\hat{\Phi}\|_2$  is not necessarily below 1, hence the RICs  $\hat{\alpha}_s$  and  $\hat{\beta}_s$  are scale-independent and can be re-scaled accordingly with  $\hat{\Phi}$ .

### 3.1. Performance Guarantees

The recovery performance of such algorithms is of our primary interest. The following theorem states the recovery error by explicitly exhibiting the component introduced by the quantization.

**Theorem 3.** *Given a noisy observation  $\mathbf{y} = \Phi\mathbf{x} + \mathbf{e}$  where  $\mathbf{y} \in \mathbb{C}^M$ ,  $\Phi \in \mathbb{C}^{M \times N}$  and  $\mathbf{x} \in \mathbb{R}^N$  is an arbitrary vector with  $\|\mathbf{x}\|_0 \leq s$ . Let  $H_s(\mathbf{x}) = \mathbf{x}^s$  with  $s \leq M$ . Assume  $\Phi$  and  $\hat{\Phi}$*

**Algorithm 1** QNIHT: Low Precision NIHT

**Input:** The set of low precision measurement matrices  $\{\hat{\Phi}_1, \hat{\Phi}_2, \dots, \hat{\Phi}_{2n^*}\}$ , measurements  $\hat{\mathbf{y}}$ , sparsity parameter  $s$ , number of iterations  $n^*$ , step size tuning parameters  $k, c$   
Initialize  $\mathbf{x}^{[0]} = 0, \Gamma^{[1]} = \text{supp}(\mathbf{H}_s(\hat{\Phi}_1^\dagger \hat{\mathbf{y}}))$ .

**for**  $n = 1$  **to**  $n^*$  **do**  
 $\mathbf{g}^{[n]} = \hat{\Phi}_{2n-1}^\dagger (\hat{\mathbf{y}} - \hat{\Phi}_{2n} \mathbf{x}^{[n]})$   
 $\hat{\mu}^{[n]} = (\mathbf{g}_{\Gamma^{[n]}}^\dagger \mathbf{g}_{\Gamma^{[n]}}) / (\mathbf{g}_{\Gamma^{[n]}}^\dagger \hat{\Phi}_{\Gamma^{[n]}}^\dagger \hat{\Phi}_{\Gamma^{[n]}} \mathbf{g}_{\Gamma^{[n]}})$   
 $\mathbf{x}^{[n+1]} = H_s(\mathbf{x}^{[n]} + \hat{\mu}^{[n]} \mathbf{g}^{[n]})$   
 $\Gamma^{[n+1]} = \text{supp}(\mathbf{x}^{[n+1]})$   
**if**  $\Gamma^{[n+1]} = \Gamma^{[n]}$   
 $\mathbf{x}^{[n+1]} = \mathbf{x}^{[n]}$   
**else if**  $\Gamma^{[n+1]} \neq \Gamma^{[n]}$   
 $b^{[n]} = (\|\mathbf{x}^{[n+1]} - \mathbf{x}^{[n]}\|_2^2) / (\|\hat{\Phi}_{2n-1}(\mathbf{x}^{[n+1]} - \mathbf{x}^{[n]})\|_2^2)$   
**if**  $\hat{\mu}^{[n]} \leq (1-c)b^{[n]}$   
 $\mathbf{x}^{[n+1]} = \mathbf{x}^{[n]}$   
**else**  $\hat{\mu}^{[n]} > (1-c)b^{[n]}$   
**repeat**  $\hat{\mu}^{[n]} \leftarrow \hat{\mu}^{[n]} / (k(1-c))$   
 $\mathbf{x}^{[n+1]} = H_s(\mathbf{x}^{[n]} + \hat{\mu}^{[n]} \mathbf{g}^{[n]})$   
**until**  $\hat{\mu}^{[n]} \leq (1-c)b^{[n]}$   
 $\Gamma^{[n+1]} = \text{supp}(\mathbf{x}^{[n+1]})$   
**end for**

satisfy the non-symmetric RIP with  $\alpha_s, \beta_s$  and  $\hat{\alpha}_s, \hat{\beta}_s$  where  $\gamma_{2s} = \beta_{2s}/\alpha_{2s} - 1 \leq 1/16$  and  $\hat{\gamma}_{2s} = \hat{\beta}_{2s}/\hat{\alpha}_{2s} - 1 \leq 1/16$ , respectively. If the normalized IHT algorithm uses low precision:

$$\mathbb{E}[\|\hat{\mathbf{x}}^{[n+1]} - \mathbf{x}^s\|_2] \leq 2^{-n} \|\mathbf{x}^s\|_2 + 10\epsilon_s + 5\epsilon_q \quad (13)$$

with  $\epsilon_s$  defined in Eqn.(9) and

$$\epsilon_q = \frac{\sqrt{M}}{\hat{\beta}_{2s}} \left( \frac{\|\mathbf{x}^s\|_2}{2^{b_\Phi-1}} + \frac{1}{2^{b_{\mathbf{y}}-1}} \right) \quad (14)$$

where  $b_\Phi$  and  $b_{\mathbf{y}}$  are the numbers of bits used to represent  $\Phi$  and  $\mathbf{y}$ , respectively.

A natural stopping criterion is  $n^* = \lceil \log_2(\|\mathbf{x}^s\|_2/\epsilon_s) \rceil$ , where the algorithm computes a successive approximation of  $\mathbf{x}^s$  with accuracy  $\mathbb{E}[\|\mathbf{x}^{[n^*]} - \mathbf{x}^s\|_2] \leq 11\epsilon_s + 5\epsilon_q$ . The error bound above is slightly simplified; our proof in the supplementary material is tighter.

**Non-symmetric RIP for  $\hat{\Phi}$**  One assumption in the the above theorem is that both the quantized problem  $\hat{\Phi}$  and the full precision problem  $\Phi$  satisfy non-symmetric RIP with  $\gamma_{2s}, \hat{\gamma}_{2s} \leq 1/16$ . The following lemma describes the relationship of the non-symmetric-RIP-ness of  $\Phi$  and  $\hat{\Phi}$ .

**Lemma 1.** Fix  $\epsilon > 0$  and let  $\Phi_\Gamma$  satisfy non-symmetric RIP with  $\gamma_{|\Gamma|} \leq 1/16 - \epsilon$  for any support set  $\Gamma$ . If the number of bits  $b$  used to represent the components of  $\Phi_\Gamma$  satisfies  $b \geq \log\left(\frac{2\sqrt{|\Gamma|}}{\epsilon\alpha_{|\Gamma|}}\right)$ , then  $\hat{\Phi}_\Gamma$  is guaranteed to satisfy  $\hat{\gamma}_{|\Gamma|} \leq 1/16$ .

We discuss procedures for obtaining quantized matrices satisfying RIP in the next section.

### 3.2. Discussion and Limitations

We examine the error bound presented in Theorem 3. Low precision IHT will asymptotically provide a sparse approximation of  $\mathbf{x}$  up to the multiples of  $\epsilon_s$  and  $\epsilon_q$  involving the noise term  $\mathbf{e}$ , the approximation error on how well  $\mathbf{x}$  can be represented by a sparse vector  $\mathbf{x}^s$  and the noise introduced by the quantization operator. Here we highlight the properties, and stress the limitations.

**Condition on  $\hat{\gamma}_{2s}$ :** In comparison to the unmodified algorithm, the condition under which the performance guarantee holds is stricter in our approach, i.e.,  $\gamma_{2s}, \hat{\gamma}_{2s} \leq 1/16$  where it was  $\gamma_{2s} \leq 1/8$  in state-of-art (Theorem 2). In applications like interferometric array imaging, this can be altered by adjusting the instrument parameters that induce  $\Phi$  and  $\hat{\Phi}$  such that  $\gamma_{2s}, \hat{\gamma}_{2s} \leq 1/16$  is satisfied. Section 2.3 of the supplementary material discusses this procedure and alternatives in detail.

When the measurement matrix  $\Phi$  is known, the condition on  $\gamma_{2s}$  can be justified by checking the singular values of  $\Phi$  which will form an upper bound on  $\gamma_{2s}$ . This is due to that singular values of submatrix is confined in the lowest and the largest singular values of its full matrix. If  $\gamma_{2s} < 1/16 - \epsilon$ , the condition on  $\hat{\gamma}_{2s}$  can be justified as follows. Let  $\sigma_i$ ,  $i \in \{1, 2, \dots, r\}$  denote the singular values of  $\Phi$ . Similarly, denote the singular values of its submatrix over the support  $\Gamma$  by  $\sigma_i^\Gamma$ , where  $|\Gamma| \leq 2s$ . Note that  $\sigma_r \leq \sigma_r^\Gamma$  and  $\sigma_1^\Gamma \leq \sigma_1$ , hence  $\alpha_{|\Gamma|} \geq \sigma_r$ . Lemma 1 further implies that the choice of number of bits  $b$  such that  $b \geq \log\left(\frac{2|\Gamma|}{\epsilon\sigma_r}\right)$  guarantees the  $\hat{\gamma}_{2s} \leq 1/16$ .

**Limitations on  $\beta_{2s}$  and  $\hat{\beta}_{2s}$ :** In normalized IHT, the measurement matrix  $\Phi$  is scale-invariant, and rigorous theoretical guarantees are achievable provided its scaling onto sparse vectors is confined in certain intervals, i.e.,  $\gamma_{2s}, \hat{\gamma}_{2s} \in [0, 1/16]$ .

The recovery error bound satisfying Eqn.(28) depends on the error term of full precision IHT:  $\epsilon_s$  and the quantization error:  $\epsilon_q$  that are inversely proportional to  $\beta_{2s}$  and  $\hat{\beta}_{2s}$ , respectively. For sufficiently large values, which compensate for  $\|\mathbf{e}\|_2$  and  $\sqrt{M}\|\mathbf{x}^s\|_2$ , the low precision approach appears competitive with the unmodified algorithm where the recovery error is bounded by  $9\epsilon_s$  in Eqn.(8). Furthermore, the scaling-invariant property of the measurement matrix  $\Phi$  permits us to scale up  $\beta_{2s}$ , hence  $\hat{\beta}_{2s}$ , by still retaining the strong recovery result similar to that of the full precision algorithm. Scaling  $\Phi$  has no effect on the condition  $\gamma_{2s}, \hat{\gamma}_{2s} \leq 1/16$ . We can have strong guarantees for recovery if the low precision algorithm operates in a regime where  $\gamma_{2s}, \hat{\gamma}_{2s} \leq 1/16$  holds.

**Comparison to other state-of-art methods:** The compressive sensing literature covers a range of algorithms, such as  $\ell_1$ -minimization, greedy and thresholding-based methods, each with its own trade-offs. In [10], CoSaMP, normalized IHT and  $\ell_1$ -minimization exhibit similar empirical performance when applied to the problems with dense Gaussian matrices. Moreover, after a simple modification of step size parameter, IHT has become compatible with these powerful methods with similar provable guarantees [11]. In the supplementary material, we show the empirical performance of low precision IHT on such synthetic examples using Gaussian measurement matrices.



### 3.3. Radio Astronomy Application

We discuss a radio astronomy application, in which radio interferometers at various locations on the ground record radio waves emitted by the celestial sources over a certain time interval, then store and process these signals to deduce a sky image. Interferometers first estimate the cross-correlation between the time series measurements, called visibilities, and then the sky image is estimated. Recently, the radio astronomy community starts to formalize the radio interferometers problems also as compressive sensing [45, 44, 30]. We directly follow this formulation.

Following in a *standard* formulation of the problem. Assume the sky is observed by employing  $L$  antennas over a stationary time interval where the earth rotation is negligible. Denote the vectorized sky image by  $\mathbf{x} \in \mathbb{R}^N$  with  $N = r^2$  where  $r$  is the resolution of images, i.e., height and width of the image in pixels. We formulate the interferometer pipeline as a compressive sensing problem such that  $\mathbf{y} = \Phi\mathbf{x} + \mathbf{e}$  where  $\Phi \in \mathbb{C}^{M \times N}$  is the measurement matrix with complex entries as a function of inner product between antenna and pixel locations,  $\mathbf{y} \in \mathbb{C}^M$  is the visibilities where  $M = L^2$ , and  $\mathbf{e} \in \mathbb{C}^M$  is the noise vector. For more background on the radio interferometer pipeline and formation of  $\Phi$ , please see Section 3 of the supplementary material.

We are able to refine our error bound for the radio astronomy scenario:

**Corollary 1.** *Let  $\sigma_n^2$  is the variance of noise introduced by a single antenna. By Theorem 3, if  $\gamma_{2s}, \hat{\gamma}_{2s} \leq 1/16$ , the low precision NIHT algorithm recovers the sky image  $\mathbf{x}^s$  with accuracy*

$$\mathbb{E}[\|\mathbf{x}^{n+1} - \mathbf{x}^s\|_2] \leq 2^{-n}\|\mathbf{x}^s\|_2 + 10\left(\frac{\sqrt{L}}{\beta_{2s}}\sigma_n + \frac{L}{\hat{\beta}_{2s}}\epsilon_{\text{sky}}\right) \quad (15)$$

where  $\epsilon_{\text{sky}} = \|\mathbf{x}^s\|_2/2^{b_\Phi} + 1/2^{b_y}$ .

**Discussion: LOFAR and Beyond.** Corollary 1 shows that the sky image can be recovered with high accuracy when certain conditions hold:  $\beta_{2s}$  and  $\hat{\beta}_{2s}$  are sufficiently large,  $\gamma_{2s}$  and  $\hat{\gamma}_{2s}$  are sufficiently small. Do these conditions hold for a real telescope? We now analyze it for one station of the LOFAR telescope, and discuss it further for radio interferometers in general.

Recall from Theorem 3 the two conditions ensuring performance guarantees: (a)  $\gamma_{2s}, \hat{\gamma}_{2s} \leq 1/16$ , (b)  $L/\hat{\beta}_{2s}$  must be large to minimize quantization error  $\epsilon_q$ . Fortunately, in the radio interferometry application, the image grid we initially form and the set of antennas used as well as scale-invariant property of normalized IHT yield us the control over  $\gamma_{2s}, \hat{\gamma}_{2s}$  and  $\beta_{2s}, \hat{\beta}_{2s}$ , respectively, through a pre-processing of  $\Phi$ . Because the measurement matrix is priorly known and can be tuned, we are able to numerically ensure that  $\gamma_{2s}, \hat{\gamma}_{2s} \leq 1/16$ . In Section 2.3 of supplementary material, we present the numerical result that proves the guarantee of this condition holds in our application.

In Fig. 3, for station CS302 of LOFAR, we first form the image grid and compute and adjust  $\Phi, \hat{\Phi}$  such that  $\gamma_{2s}, \hat{\gamma}_{2s} \leq 1/16$  holds. Then we numerically compute the scaling factors of errors  $\sigma_n$  and  $\epsilon_{\text{sky}}$ :  $\sqrt{L}/\beta_{2s}$  and  $L/\hat{\beta}_{2s}$ , respectively. Theorem 3 states that the recovery error is induced by two terms:  $\sqrt{L}/\beta_{2s}$  and  $L/\hat{\beta}_{2s}$ . Therefore, we investigate these scaling over various antenna numbers and sparsity level. The results suggest that 2-bits IHT has a negligible quantization error when applied radio interferometry imaging problem.

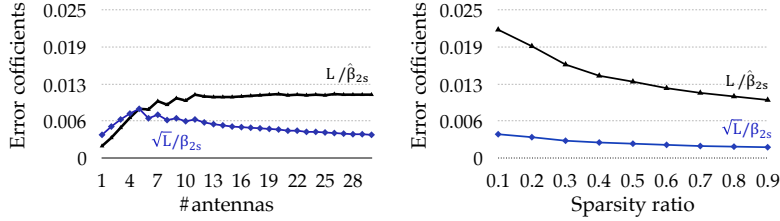


FIG 3. Monitoring the error coefficients:  $\sqrt{L}/\beta_{2s}$  and  $L/\hat{\beta}_{2s}$  that scale  $\sigma_n$  and  $\|\mathbf{x}^s\|_2$  that appear in the recovery error bound, respectively. Sparsity ratio stands for  $s/M$ . The numerical value of coefficients guarantees that  $\|\mathbf{x}^{[n+1]} - \mathbf{x}^s\|_2 / \|\mathbf{x}^s\|_2$  is sufficiently small regardless of the number of bits to represent  $\Phi$ .

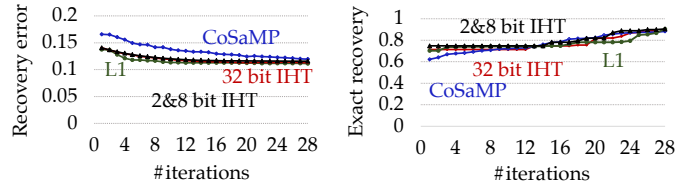


FIG 4. Comparison of recovery error and exact recovery (support) for various methods.

#### 4. Experimental Results

We assess the empirical performance of our approach using the radio interferometer measurements from a real telescope: the LOw Frequency ARray (LOFAR). We first demonstrate that the accuracy achieved in the low precision setting is comparable with high precision IHT and other state-of-art methods; we then show the speed-up of wall-clock time.

**Accuracy.** We recover the full sky image of the resolution  $256 \times 256$  pixels ( $\mathbf{x} \in \mathbb{R}^{65,536}$  in vectorized form) by employing 30 low-band antennas of LOFAR CS302 station that operates in 15-80 MHz frequency band where the sky is populated with 30 strong sources, that is,  $\mathbf{y} \in \mathbb{C}^{900}$ ,  $\hat{\Phi} \in \mathbb{C}^{900 \times 65,536}$ . The SNR is 0 dB at the antenna level, i.e.,  $10 \log_{10}(\|\Phi \mathbf{x}\|_2^2 / \|\mathbf{e}\|_2^2) = 0$  dB.

**Improving least square estimates.** Fig. 1 provides an example of sky recoveries: (a) ground truth estimated over 12 hours of observation, (b) a least square estimate of underlying sky (or dirty image in the nomenclature of radio astronomy), (c) 32 bit and (d) 2&8 bit (normalized) IHT which uses 2 bits for the measurement matrix and 8 bits for the observation. This experiment indicates that low precision IHT captures the sky sources successfully even when only 2 bit are used to compress  $\Phi$ . Thus, we can drastically reduce the data precision yet still estimate the sky precisely.

**Comparison to state-of-art methods.** We compare low precision IHT to full precision IHT, CoSaMP and an  $\ell_1$ -based approach in terms of their capability to recover sparse signals. For this particular formulation of the interferometric imaging problem, they can iteratively build up an estimate of the sky map  $\mathbf{x}$ . To avoid bias towards any algorithm, we optimized each algorithm independently.

We first evaluate algorithms through two metrics: (1) the recovery error and (2) exact recovery, that is, the ratio of support that is successfully recovered. In radio interferometry, however, it is customary to use number of true celestial sources resolved in the recovered image as a performance metric, i.e., true-positive findings. That is, the performance of the algorithms is no longer described by its ability to recover support entirely but the sky objects, which possess higher error tolerance. We demonstrate in Fig. 4 that IHT performs as well as its alternatives and compatible to  $\ell_1$ -minimization in terms of its exact recovery performance. Empirical results suggest that the celestial sources can still be recovered when dramatically quantizing  $\Phi$ . This experiment is informative merely on the accuracy of the results obtained implementing these alternative algorithms. A fair comparison involves the analysis of different properties such as speed and storage requirements, flexibility and ease of implementation. IHT is known to outperform CoSaMP when  $\Phi$  has similar entries in magnitude [11], which is confirmed by our experiments. Empirical evidence further suggests that IHT performs nearly as well as the  $\ell_1$ -based approach. The low precision approach has similar recovery performance as high precision IHT, as shown in Fig. 4.

**System Speed-up.** We demonstrate the speed up for performing IHT using low precision on both CPUs and FPGAs. We leave the implementation details to the supplementary material. We validate our algorithm on both radio astronomy data (here) and synthetic data sets (in supplementary material).

**FPGA Speed-up.** The performance of the FPGA-based system is presented in Fig. 6. For the time spent per iteration, we see that quantization, and the resulting compression of the measurement matrix  $\Phi$  leads to near linear speed up for recovering the support vector. All variants (full precision to lowest precision) of IHT on FPGA can consume  $\Phi$  at the same rate, and therefore the runtime of IHT depends linearly on the size of  $\Phi$ , leading to linear speed ups that we observe in the experiments. In terms of end-to-end performance, we measure the time for each precision level needs to reach support recovery ratio 90% and calculate the speedup. The 2&8-bit IHT variant reaches the same support recovery ratio 9.19× faster.

**CPU Speed-up.** Our CPU implementation uses handwritten code in AVX2 intrinsics and supports 4-bit, 8-bit, and 32-bit precisions. We take advantage of the sparsity of the  $x$  vectors whenever possible. The bulk of the computation is accounted for by two routines: A matrix-vector multiplication which for 4-bit and 8-bit casts its computation in terms of dot-products, and a matrix times a sparse vector, which for all three datatypes casts its computation in terms of a dense scale-and-add routine. On real astronomical data, we obtain a 2.84× speed-up for the 8-bit implementation, and of 4.19× for the 4-bit implementation, with similar recovery properties as for the FPGA.

## 5. Discussion

We investigated low precision schemes to sparse signal recovery problems, and introduced a low-precision NIHT variant, with theoretical guarantees and good practical performance, both in terms of accuracy and recovery time, validated for a real radio astronomy application, with both CPU and FPGA implementations. In future work, we plan to explore

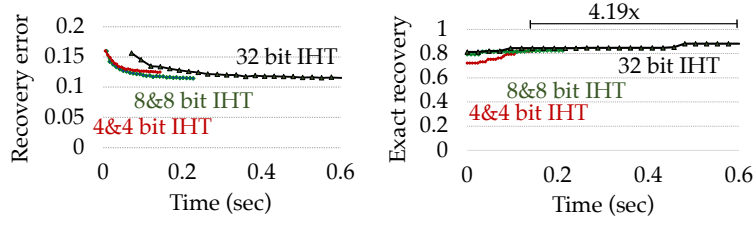


FIG 5. Speed-up of low precision IHT on CPU 4-bit and 8-bit. The 8-bit end-to-end speed-up is of  $\simeq 3\times$ , while the 4-bit end-to-end speed-up is of  $\simeq 4\times$ .

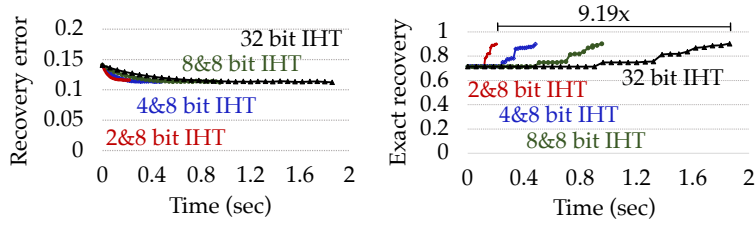


FIG 6. Speed-up of low precision IHT on FPGA. 2&8 bit IHT provides 9.19 $\times$  speedup versus full-precision.

algorithms which work with end-to-end low precision data representation, and extending these techniques to other greedy recovery algorithms, and sparse recovery frameworks.

## Contents

1	Introduction . . . . .	1
2	Preliminaries . . . . .	4
3	Low Precision Iterative Thresholding . . . . .	5
	3.1 Performance Guarantees . . . . .	6
	3.2 Discussion and Limitations . . . . .	8
	3.3 Radio Astronomy Application . . . . .	9
4	Experimental Results . . . . .	10
5	Discussion . . . . .	11
6	Proofs . . . . .	13
	6.1 Preliminaries . . . . .	13
	6.2 Proof of Theorem 3 . . . . .	16
	6.3 Proof of Lemma 1 . . . . .	19
7	Radio Interferometer Pipeline . . . . .	20
	7.1 Basic Data Model . . . . .	20
	7.2 Formation of $\Phi$ . . . . .	24
	7.3 How we satisfy conditions on Restricted Isometry Property? . . . . .	24
	7.4 Performance Analysis with NIHT . . . . .	25
	7.5 Inverse Fourier transform combined with CLEAN algorithm . . . . .	26
8	FPGA Implementation Details . . . . .	27
	8.1 Performance analysis . . . . .	28
	8.2 Computing $\Phi$ on the fly . . . . .	29
9	CPU Implementation Details . . . . .	29
10	Toy Example: Gaussian Data . . . . .	29
	References . . . . .	30

## 6. Proofs

### 6.1. Preliminaries

We begin by introducing our notation.

1.  $\mathbf{y} = \Phi \mathbf{x} + \mathbf{e} = \Phi \mathbf{x}^s + \Phi(\mathbf{x} - \mathbf{x}^s) + \mathbf{e}$ ,
2.  $\boldsymbol{\varepsilon} = \Phi(\mathbf{x} - \mathbf{x}^s) + \mathbf{e}$ , hence  $\mathbf{y} = \Phi \mathbf{x}^s + \boldsymbol{\varepsilon}$ ,
3.  $\boldsymbol{\varepsilon}_{\mathbf{y}} = Q(\mathbf{y}, b) - \mathbf{y}$ ,
4.  $\Gamma^{[n]} = \text{supp}\{\mathbf{x}^{[n]}\}$ ,  $\hat{\Gamma}^{[n]} = \text{supp}\{\hat{\mathbf{x}}^{[n]}\}$  and  $\Gamma^s = \text{supp}\{\mathbf{x}^s\}$ ,
5.  $B^{[n]} = \Gamma^{[n]} \cup \Gamma^s$  and  $\hat{B}^{[n]} = \hat{\Gamma}^{[n]} \cup \Gamma^s$ ,
6.  $\mathbf{a}^{[n+1]} = \hat{\mathbf{x}}^{[n]} + \mu^{[n]} \Phi^\dagger(\mathbf{y} - \Phi \hat{\mathbf{x}}^{[n]})$  and  $\hat{\mathbf{a}}^{[n+1]} = \hat{\mathbf{x}}^{[n]} + \hat{\mu}^{[n]} Q_1(\Phi)^\dagger(\mathbf{y} - Q_2(\Phi) \hat{\mathbf{x}}^{[n]})$ ,
7.  $\mathbf{x}^{[n+1]} = H_s(\mathbf{a}^{[n+1]})$  and  $\hat{\mathbf{x}}^{[n+1]} = H_s(\hat{\mathbf{a}}^{[n+1]})$ ,
8.  $\mathbf{r}^{[n]} = \hat{\mathbf{x}}^{[n]} - \mathbf{x}^s$ .

Assume  $\Phi$  satisfies the non-symmetric Restricted Isometry Property

$$\alpha_s \leq \frac{\|\Phi \mathbf{x}\|_2}{\|\mathbf{x}\|_2} \leq \beta_s \quad (16)$$

for all  $\mathbf{x} : \|\mathbf{x}\|_0 \leq s$ , where  $\alpha_s \in \mathbb{R}$  and  $\beta_s \in \mathbb{R}$  are the lowest and largest singular value of  $\Phi$  such that  $0 < \alpha_s \leq \beta_s$ , the so-called restricted isometric constants. Inherent from its definition, the restricted isometry holds for the quantized measurement matrix denoted by  $Q(\Phi, b_m)$  such that

$$\hat{\alpha}_s \leq \frac{\|Q(\Phi, b_m)\mathbf{x}\|_2}{\|\mathbf{x}\|_2} \leq \hat{\beta}_s \quad (17)$$

where  $\hat{\alpha}_s$  and  $\hat{\beta}_s$  are associated restricted isometry constants. For simplicity, we drop  $b_m$ , and use  $Q(\Phi)$  instead. Also, let  $\gamma_s = \max\{1 - \alpha_s/\beta_s, \beta_s/\alpha_s - 1\}$  and  $\hat{\gamma}_s = \max\{1 - \hat{\alpha}_s/\hat{\beta}_s, \hat{\beta}_s/\hat{\alpha}_s - 1\}$ .

**Remark 2.** *The adaptive setting of step size parameter  $\mu^{[n]}$  and  $\hat{\mu}^{[n]}$  in normalized IHT is shown to satisfy  $1/\beta_{2s}^2 \leq \mu^{[n]} \leq 1/\alpha_{2s}^2$  and  $1/\hat{\beta}_{2s}^2 \leq \hat{\mu}^{[n]} \leq 1/\hat{\alpha}_{2s}^2$ . Using the definitions of  $\gamma_s$  and  $\hat{\gamma}_s$ , we further have*

$$(1 - \gamma_{2s})/\alpha_{2s}^2 \leq \mu^{[n]} \leq (1 + \gamma_{2s})/\beta_{2s}^2, \quad (18)$$

$$(1 - \hat{\gamma}_{2s})/\hat{\alpha}_{2s}^2 \leq \hat{\mu}^{[n]} \leq (1 + \hat{\gamma}_{2s})/\hat{\beta}_{2s}^2. \quad (19)$$

Based on the properties above, the restricted isometry and the adaptive step size, which we will require repeatedly throughout the proof, has several other consequences, summarized as follows.

**Lemma 2.** *Suppose  $\Phi$  and  $Q(\Phi)$  satisfy restricted isometry property in Eqns.16&17. Then*

$$\|(\mu^{[n]}\Phi_\Gamma^T - \hat{\mu}^{[n]}Q(\Phi)_\Gamma^T)\mathbf{x}_\Gamma\|_2 \leq \max((1 + \gamma_{|\Gamma|})/\beta_{|\Gamma|}, 1 + \hat{\gamma}_{|\Gamma|})\|\mathbf{x}_\Gamma\|_2, \quad (20)$$

$$\|(\mu^{[n]}\Phi_\Gamma^T\Phi_\Gamma - \mu^{[n]}Q_1(\Phi)_\Gamma^TQ_2(\Phi)_\Gamma)\mathbf{x}_\Gamma\|_2 \leq (\gamma_{|\Gamma|} + \hat{\gamma}_{|\Gamma|})\|\mathbf{x}_\Gamma\|_2, \quad (21)$$

$$\|(\mu^{[n]}\Phi_\Upsilon^T\Phi_\Lambda - \mu^{[n]}Q_1(\Phi)_\Upsilon^TQ_2(\Phi)_\Lambda)\mathbf{x}_\Lambda\|_2 \leq \max(\gamma_{|\Upsilon \cup \Lambda|}, \hat{\gamma}_{|\Upsilon \cup \Lambda|})\|\mathbf{x}_\Lambda\|_2. \quad (22)$$

*Proof.* As a simple consequence of restricted isometry property, the singular values of  $\Phi_\Gamma$  lie between  $\alpha_{|\Gamma|}$  and  $\beta_{|\Gamma|}$ . Eqn.18&19 further imply that the singular values of  $\mu^{[n]}\Phi_\Gamma$  are in  $[(1 - \gamma_{|\Gamma|})/\alpha_{|\Gamma|}, (1 + \gamma_{|\Gamma|})/\beta_{|\Gamma|}]$ . Using the similar bound for  $Q(\Phi)_\Gamma$ , maximum singular value of  $(\mu^{[n]}\Phi_\Gamma^T - \hat{\mu}^{[n]}Q(\Phi)_\Gamma^T)$ , i.e., its operator norm, is given by  $(1 + \gamma_{|\Gamma|})/\beta_{|\Gamma|} - (1 - \hat{\gamma}_{|\Gamma|})/\alpha_{|\Gamma|}$ . In Eqn.20, we use a looser bound  $(1 + \gamma_{|\Gamma|})/\beta_{|\Gamma|}$  for simplicity.

Similar argument holds for Eqn.21, that is, the singular values of  $\mu^{[n]}\Phi_\Gamma^T\Phi_\Gamma$  and  $\mu^{[n]}Q_1(\Phi)_\Gamma^TQ_2(\Phi)_\Gamma$  fall into  $[1 - \gamma_{|\Gamma|}, 1 + \gamma_{|\Gamma|}]$  and  $[1 - \hat{\gamma}_{|\Gamma|}, 1 + \hat{\gamma}_{|\Gamma|}]$ , respectively. Then  $\|\mu^{[n]}\Phi_\Gamma^T\Phi_\Gamma - \mu^{[n]}Q_1(\Phi)_\Gamma^TQ_2(\Phi)_\Gamma\|_2$  is bounded by  $\gamma_{|\Gamma|} + \hat{\gamma}_{|\Gamma|}$ , which proves Eqn. 21.

Eqn. 22 is a consequence of the fact that  $-\mu^{[n]}\Phi_\Upsilon^T\Phi_\Lambda$  is a submatrix of  $I - \mu^{[n]}\Phi_{\Upsilon \cup \Lambda}^T\Phi_{\Upsilon \cup \Lambda}$ , which in turn implies that  $\|\mu^{[n]}\Phi_\Upsilon^T\Phi_\Lambda\|_2 \leq \|I - \mu^{[n]}\Phi_{\Upsilon \cup \Lambda}^T\Phi_{\Upsilon \cup \Lambda}\|_2$ , (i.e., spectral norm of a submatrix is bounded by the norm of its full matrix, and moreover, spectral norm is equivalent to operator norm in our setting). As previously shown, eigenvalues of  $\mu^{[n]}\Phi_{\Upsilon \cup \Lambda}^T\Phi_{\Upsilon \cup \Lambda}$  lie in  $[1 - \gamma_{|\Upsilon \cup \Lambda|}, 1 + \gamma_{|\Upsilon \cup \Lambda|}]$ . Hence, eigenvalues of  $\mu^{[n]}\Phi_\Upsilon^T\Phi_\Lambda$  are in  $[0, \gamma_{|\Upsilon \cup \Lambda|}]$ . The maximum eigen value of  $(\mu^{[n]}\Phi_\Upsilon^T\Phi_\Lambda - \mu^{[n]}Q_1(\Phi)_\Upsilon^TQ_2(\Phi)_\Lambda)$ , hence its operator norm, can then be bounded by  $\max(\gamma_{|\Upsilon \cup \Lambda|}, \hat{\gamma}_{|\Upsilon \cup \Lambda|})$ .  $\square$

**Lemma 3.** [10] For any  $\mathbf{x}$ , let  $\mathbf{x}^s$  be the best  $s$ -term approximation to  $\mathbf{x}$  and  $\Upsilon$  be a set with at most  $s$  elements. Then

$$\|\mu^{[n]} \Phi_{\Upsilon}^T \Phi(\mathbf{x} - \mathbf{x}^s)\|_2 \leq (1 + \gamma_{2|\Upsilon|}) [\|\mathbf{x} - \mathbf{x}^s\|_2] + \frac{\|\mathbf{x} - \mathbf{x}^s\|_2}{\sqrt{s}}. \quad (23)$$

**Lemma 4.** Let  $Q(\cdot, b) : \mathbb{R}^M \times \mathbb{Z}^+ \rightarrow \mathbb{R}^d$  denote quantization operator described in the paper. For any  $\mathbf{v} \in \mathbb{R}^d$ , the norm of quantization error can be bounded by

$$\mathbb{E}[\|Q(\mathbf{v}, b) - \mathbf{v}\|_2] \leq \frac{c_v \sqrt{M}}{2^{b-1}} \quad (24)$$

where  $c_v$  is the maximum value of the components of  $\mathbf{v}$  in magnitude.

**Remark 3.** For efficient fixed-point computation on Field Programmable Gate Array, we need an odd number of quantization levels, and therefore total number of levels for  $b$  bit quantization is  $2^{b-1} + 1$ . That is, the interval between two consecutive levels is  $2^{b-1}$  provided the values are confined in the interval  $[-1, 1]$  a priori.

*Proof.* Let  $\tilde{\mathbf{v}} = \mathbf{v}/c_v$ . Using Jensen's inequality we can easily show that

$$\begin{aligned} \mathbb{E}[\|Q(\tilde{\mathbf{v}}, b) - \tilde{\mathbf{v}}\|_2] &\leq \sqrt{\mathbb{E}[\|Q(\tilde{\mathbf{v}}, b) - \tilde{\mathbf{v}}\|_2^2]} = \sqrt{\sum_{i=1}^M \mathbb{E}[(Q(\tilde{\mathbf{v}}, b)_i - \tilde{v}_i)^2]} \\ &\leq \sqrt{\sum_{i=1}^M \mathbb{P}(Q(\tilde{\mathbf{v}}, b)_i = \ell_j)(\tilde{v}_i - \ell_j)^2 + \mathbb{P}(Q(\tilde{\mathbf{v}}, b)_i = \ell_{j+1})(\ell_{j+1} - \tilde{v}_i)^2}. \end{aligned} \quad (25)$$

Our quantization scheme uses a stochastic approach such that  $\mathbb{P}(Q(\hat{\mathbf{v}}, b)_i = \ell_j) = \frac{\ell_{j+1} - \tilde{v}_i}{\ell_{j+1} - \ell_j}$ , and hence  $\mathbb{P}(Q(\tilde{\mathbf{v}}, b)_i = \ell_{j+1}) = 1 - \frac{\ell_{j+1} - \tilde{v}_i}{\ell_{j+1} - \ell_j}$ . Substituting these into Eqn. 25 we have

$$\mathbb{E}[\|Q(\tilde{\mathbf{v}}, b) - \tilde{\mathbf{v}}\|_2] \leq \sqrt{\sum_{i=1}^n (\ell_{j+1} - Q(\tilde{\mathbf{v}}, b)_i)(Q(\tilde{\mathbf{v}}, b)_i - \ell_j)}. \quad (26)$$

It can easily be seen that  $(\ell_{j+1} - Q(\hat{\mathbf{v}}, b)_i)(Q(\hat{\mathbf{v}}, b)_i - \ell_j)$  is maximized when  $Q(\hat{\mathbf{v}}, b)_i = \frac{\ell_{j+1} - \ell_j}{2}$ , moreover quantization function implies that  $\ell_{j+1} - \ell_j = \frac{1 - (-1)}{l} = \frac{1}{2^{b-2}}$

$$\mathbb{E}[\|Q(\tilde{\mathbf{v}}, b) - \tilde{\mathbf{v}}\|_2] \leq \sqrt{\sum_{i=1}^M \frac{(\ell_{j+1} - \ell_j)^2}{4}} \leq \frac{\sqrt{M}(\ell_{j+1} - \ell_j)}{2} \leq \frac{\sqrt{M}}{2^{b-1}}. \quad (27)$$

□

### 6.2. Proof of Theorem 3

The recovery error can be split into two parts by using triangle inequality

$$\begin{aligned} \mathbb{E}[\|\hat{\mathbf{x}}^{[n+1]} - \mathbf{x}^s\|_2 | \hat{\mathbf{x}}^{[n]}] &= \mathbb{E}[\|\hat{\mathbf{x}}_{B^{[n+1]}}^{[n+1]} - \mathbf{x}_{B^{[n+1]}}^s\|_2 | \hat{\mathbf{x}}^{[n]}] \\ &\leq \mathbb{E}[\|\hat{\mathbf{x}}_{B^{[n+1]}}^{[n+1]} - \hat{\mathbf{a}}_{B^{[n+1]}}^{[n+1]}\|_2 | \hat{\mathbf{x}}^{[n]}] + \mathbb{E}[\|\hat{\mathbf{a}}_{B^{[n+1]}}^{[n+1]} - \mathbf{x}_{B^{[n+1]}}^s\|_2 | \hat{\mathbf{x}}^{[n]}]. \end{aligned} \quad (28)$$

where the equality follows from that  $\hat{\mathbf{x}}^{[n+1]} - \mathbf{x}^s$  is supported over the set  $B^{[n+1]} = \hat{\Gamma}^{[n+1]} \cup \Gamma^s$ .

Recall that  $\hat{\mathbf{x}}_{B^{[n+1]}}^{[n+1]}$  is a better  $s$ -term approximation to  $\hat{\mathbf{a}}_{B^{[n+1]}}^{[n+1]}$  than  $\mathbf{x}_{B^{[n+1]}}^s$  (i.e.,  $\|\hat{\mathbf{x}}_{B^{[n+1]}}^{[n+1]} - \hat{\mathbf{a}}_{B^{[n+1]}}^{[n+1]}\|_2 \leq \|\hat{\mathbf{a}}_{B^{[n+1]}}^{[n+1]} - \mathbf{x}_{B^{[n+1]}}^s\|_2$ ). Then

$$\mathbb{E}[\|\hat{\mathbf{x}}^{[n+1]} - \mathbf{x}^s\|_2 | \hat{\mathbf{x}}^{[n]}] \leq 2\mathbb{E}[\|\hat{\mathbf{a}}_{B^{[n+1]}}^{[n+1]} - \mathbf{x}_{B^{[n+1]}}^s\|_2 | \hat{\mathbf{x}}^{[n]}]. \quad (29)$$

Using triangle inequality, we further have

$$\mathbb{E}[\|\hat{\mathbf{x}}^{[n+1]} - \mathbf{x}^s\|_2 | \hat{\mathbf{x}}^{[n]}] \leq 2[\mathbb{E}[\|\hat{\mathbf{a}}_{B^{[n+1]}}^{[n+1]} - \mathbf{a}_{B^{[n+1]}}^{[n+1]}\|_2 + \|\mathbf{a}_{B^{[n+1]}}^{[n+1]} - \mathbf{x}_{B^{[n+1]}}^s\|_2 | \hat{\mathbf{x}}^{[n]}]] \quad (30)$$

We now continue with the analysis referring to two terms on the right hand side of Eqn. 30 separately.

(a) Expanding  $\hat{\mathbf{a}}_{B^{[n+1]}}^{[n+1]}$  and  $\mathbf{a}_{B^{[n+1]}}^{[n+1]}$  we have

$$\begin{aligned} &\mathbb{E}[\|\hat{\mathbf{a}}_{B^{[n+1]}}^{[n+1]} - \mathbf{a}_{B^{[n+1]}}^{[n+1]}\|_2 | \hat{\mathbf{x}}^{[n]}] \\ &= \mathbb{E}[\|\hat{\mu}^{[n]} Q_1(\Phi)_{B^{[n+1]}}^T (Q_y(\mathbf{y}) - Q_2(\Phi)\hat{\mathbf{x}}^{[n]}) - \mu^{[n]} \Phi_{B^{[n+1]}}^T (\mathbf{y} - \Phi\hat{\mathbf{x}}^{[n]})\|_2 | \hat{\mathbf{x}}^{[n]}] \\ &= \mathbb{E}[\|\hat{\mu}^{[n]} Q_1(\Phi)_{B^{[n+1]}}^T (\Phi\mathbf{x}^s + \varepsilon + \epsilon_y - Q_2(\Phi)\hat{\mathbf{x}}^{[n]}) - \mu^{[n]} \Phi_{B^{[n+1]}}^T (\Phi\mathbf{x}^s + \varepsilon - \Phi\hat{\mathbf{x}}^{[n]})\|_2 | \hat{\mathbf{x}}^{[n]}] \\ &= \mathbb{E}[\|\hat{\mu}^{[n]} Q_1(\Phi)_{B^{[n+1]}}^T (-Q_2(\Phi)\mathbf{r}^{[n]} + \varepsilon + \epsilon_y + (\Phi - Q_2(\Phi))\mathbf{x}^s) + \mu^{[n]} \Phi_{B^{[n+1]}}^T (\Phi\mathbf{r}^{[n]} - \varepsilon)\|_2 | \hat{\mathbf{x}}^{[n]}] \\ &\leq \|(\mu^{[n]} \Phi_{B^{[n+1]}}^T \Phi - \hat{\mu}^{[n]} Q_1(\Phi)_{B^{[n+1]}}^T Q_2(\Phi))\mathbf{r}^{[n]}\|_2 \\ &\quad + \|(\mu^{[n]} \Phi_{B^{[n+1]}}^T - \hat{\mu}^{[n]} Q_1(\Phi)_{B^{[n+1]}}^T)\varepsilon\|_2 \\ &\quad + \mathbb{E}[\|\hat{\mu}^{[n]} Q_1(\Phi)_{B^{[n+1]}}^T \epsilon_y\|_2] \\ &\quad + \mathbb{E}[\|\hat{\mu}^{[n]} Q_1(\Phi)_{B^{[n+1]}}^T (\Phi - Q_2(\Phi))\mathbf{x}^s\|_2]. \end{aligned} \quad (31)$$

where we used the expansion  $\mathbf{r}^{[n]} = \hat{\mathbf{x}}^{[n]} - \mathbf{x}^s$ . We further derive the terms governing the above expression in (a.1), (a.2), (a.3) and (a.4).

(a.1) Since  $\mathbf{r}^{[n]}$  is supported over  $B^{[n]}$ , we clearly have

$$\begin{aligned} &\|(\mu^{[n]} \Phi_{B^{[n+1]}}^T \Phi - \hat{\mu}^{[n]} Q_1(\Phi)_{B^{[n+1]}}^T Q_2(\Phi))\mathbf{r}^{[n]}\|_2 \\ &\leq \|(\mu^{[n]} \Phi_{B^{[n+1]}}^T \Phi_{B^{[n+1]}} - \hat{\mu}^{[n]} Q_1(\Phi)_{B^{[n+1]}}^T Q_2(\Phi)_{B^{[n+1]}})\mathbf{r}_{B^{[n+1]}}^{[n]}\|_2 \\ &\quad + \|(\mu^{[n]} \Phi_{B^{[n+1]}}^T \Phi_{B^{[n]} \setminus B^{[n+1]}} - \hat{\mu}^{[n]} Q_1(\Phi)_{B^{[n+1]}}^T Q_2(\Phi)_{B^{[n]} \setminus B^{[n+1]}})\mathbf{r}_{B^{[n]} \setminus B^{[n+1]}}^{[n]}\|_2. \end{aligned} \quad (32)$$



Using Eqn. 21 we have

$$\|(\mu^{[n]}\Phi_{B^{[n+1]}}^T\Phi_{B^{[n+1]}} - \hat{\mu}^{[n]}Q_1(\Phi)_{B^{[n+1]}}^TQ_2(\Phi)_{B^{[n+1]}})\mathbf{r}_{B^{[n+1]}}^{[n]}\|_2 \leq (\gamma_{2s} + \hat{\gamma}_{2s})\|\mathbf{r}_{B^{[n+1]}}^{[n]}\|_2. \quad (33)$$

Let now  $B^{[n+1]}$  be split into two disjoint sets  $\Gamma_1$  and  $\Gamma_2$ , where  $\Gamma_1 \cap \Gamma_2 = \emptyset$  and  $|\Gamma_1|, |\Gamma_2| \leq s$ . We have by Eqn.22

$$\begin{aligned} \|(\mu^{[n]}\Phi_{B^{[n+1]}}^T\Phi_{B^{[n+1]}\setminus B^{[n]}} - \hat{\mu}^{[n]}Q_1(\Phi)_{B^{[n+1]}\setminus B^{[n]}}^TQ_2(\Phi)_{B^{[n+1]}\setminus B^{[n]}})\mathbf{r}_{B^{[n+1]}\setminus B^{[n]}}^{[n]}\|_2 \leq \\ \left( \|(\mu^{[n]}\Phi_{\Gamma_1}^T\Phi_{B^{[n+1]}\setminus B^{[n]}} - \hat{\mu}^{[n]}Q_1(\Phi)_{\Gamma_1}^TQ_2(\Phi)_{B^{[n+1]}\setminus B^{[n]}})\mathbf{r}_{B^{[n+1]}\setminus B^{[n]}}^{[n]}\|_2^2 \right. \\ \left. + \|(\mu^{[n]}\Phi_{\Gamma_2}^T\Phi_{B^{[n+1]}\setminus B^{[n]}} - \hat{\mu}^{[n]}Q_1(\Phi)_{\Gamma_2}^TQ_2(\Phi)_{B^{[n+1]}\setminus B^{[n]}})\mathbf{r}_{B^{[n+1]}\setminus B^{[n]}}^{[n]}\|_2^2 \right)^{\frac{1}{2}} \\ \leq \sqrt{2} \max(\gamma_{2s}, \hat{\gamma}_{2s})\|\mathbf{r}_{B^{[n+1]}\setminus B^{[n]}}^{[n]}\|_2. \end{aligned} \quad (34)$$

(a.1) Combining Eqn.33 & 34,

$$\begin{aligned} \|(\mu^{[n]}\Phi_{B^{[n+1]}}^T\Phi - \hat{\mu}^{[n]}Q_1(\Phi)_{B^{[n+1]}}^TQ_2(\Phi))\mathbf{r}^{[n]}\|_2 \\ = (\gamma_{2s} + \hat{\gamma}_{2s})\|\mathbf{r}_{B^{[n+1]}}^{[n]}\|_2 + \sqrt{2} \max(\gamma_{2s}, \hat{\gamma}_{2s})\|\mathbf{r}_{B^{[n+1]}\setminus B^{[n]}}^{[n]}\|_2 \\ \leq 2 \max(\gamma_{2s}, \hat{\gamma}_{2s})\|\mathbf{r}^{[n]}\|_2 \end{aligned} \quad (35)$$

where the last inequality follows from the fact that  $\mathbf{r}_{B^{[n+1]}}^{[n]}$  and  $\mathbf{r}_{B^{[n+1]}\setminus B^{[n]}}^{[n]}$  are orthogonal.

(a.2) Expanding the second term in Eqn. 31

$$\begin{aligned} \|(\mu^{[n]}\Phi_{B^{[n+1]}} - \hat{\mu}^{[n]}Q_1(\Phi)_{B^{[n+1]}}^T)\boldsymbol{\varepsilon}\|_2 \\ \leq \|(\mu^{[n]}\Phi_{B^{[n+1]}} - \hat{\mu}^{[n]}Q_1(\Phi)_{B^{[n+1]}}^T)\mathbf{e}\|_2 + \|(\mu^{[n]}\Phi_{B^{[n+1]}} - \hat{\mu}^{[n]}Q_1(\Phi)_{B^{[n+1]}}^T)\Phi(\mathbf{x} - \mathbf{x}^s)\|_2. \end{aligned} \quad (36)$$

Using Eqn.23, 20 & 21 we have

$$\begin{aligned} \|(\mu^{[n]}\Phi_{B^{[n+1]}} - \hat{\mu}^{[n]}Q_1(\Phi)_{B^{[n+1]}}^T)\mathbf{e}\|_2 \leq \max((1 + \gamma_{2s})/\beta_{2s}, (1 + \hat{\gamma}_{2s})/\hat{\beta}_{2s})\|\mathbf{e}\|_2 \\ \|(\mu^{[n]}\Phi_{B^{[n+1]}} - \hat{\mu}^{[n]}Q_1(\Phi)_{B^{[n+1]}}^T)\Phi(\mathbf{x} - \mathbf{x}^s)\|_2 \\ \leq (\|\mu^{[n]}\Phi_{\Gamma_1} - \hat{\mu}^{[n]}Q_1(\Phi)_{\Gamma_1}^T\|_2^2 + \|(\mu^{[n]}\Phi_{\Gamma_2} - \hat{\mu}^{[n]}Q_1(\Phi)_{\Gamma_2}^T)\Phi(\mathbf{x} - \mathbf{x}^s)\|_2^2)^{1/2} \\ \leq \sqrt{2} \max(\hat{\gamma}_{2s}, \hat{\gamma}_{2s}) \left[ \|\mathbf{x} - \mathbf{x}^s\|_2 + \frac{\|\mathbf{x} - \mathbf{x}^s\|_1}{\sqrt{s}} \right]. \end{aligned} \quad (37)$$

(a.3) Combining results obtained in Eqn. 37

$$\begin{aligned} \|(\mu^{[n]}\Phi_{B^{[n+1]}} - \hat{\mu}^{[n]}Q_1(\Phi)_{B^{[n+1]}}^T)\boldsymbol{\varepsilon}\|_2 \leq \max((1 + \gamma_{2s})/\beta_{2s}, (1 + \hat{\gamma}_{2s})/\hat{\beta}_{2s})\|\mathbf{e}\|_2 \\ + \sqrt{2} \max(\hat{\gamma}_{2s}, \hat{\gamma}_{2s}) \left[ \|\mathbf{x} - \mathbf{x}^s\|_2 + \frac{\|\mathbf{x} - \mathbf{x}^s\|_1}{\sqrt{s}} \right]. \end{aligned} \quad (38)$$

The third term of Eqn.31

$$\begin{aligned} \mathbb{E}[\|\hat{\mu}^{[n+1]}Q_1(\Phi)_{B^{[n+1]}}^T \epsilon_y\|_2] &\stackrel{(1)}{\leq} \frac{(1 + \hat{\gamma}_{2s})}{\hat{\beta}_{2s}} \mathbb{E}[\|\epsilon_y\|_2] \\ &\stackrel{(2)}{\leq} \frac{(1 + \hat{\gamma}_{2s})c_y\sqrt{M}}{\hat{\beta}_{2s}2^{b_y-1}}. \end{aligned} \quad (39)$$

where the inequalities follows from (1) Eqn. 17 & ??, and (2) Lemma 4.

(a.4) Combining with Eqn. 17 & ??, *Cauchy-Bunyakovsky-Schwarz*, *Jensen* inequalities and the similar discussion above

$$\begin{aligned} \mathbb{E}[\|\hat{\mu}^{[n]}Q_1(\Phi)_{B^{[n+1]}}^T (\Phi - Q_2(\Phi))\mathbf{x}^s\|_2] &\leq \frac{(1 + \hat{\gamma}_{2s})}{\hat{\beta}_{2s}} \mathbb{E}[\|(\Phi - Q_2(\Phi))\mathbf{x}^s\|_2] \\ &\leq \frac{(1 + \hat{\gamma}_{2s})}{\hat{\beta}_{2s}} \sqrt{\sum_i^M \sum_j^N \mathbb{E}[(\Phi_{i,j} - Q_2(\Phi_{i,j})\mathbf{x}_j^s)^2]} \quad (40) \\ &= \frac{(1 + \hat{\gamma}_{2s})c_\Phi\sqrt{M}}{\hat{\beta}_{2s}2^{b_\Phi-1}} \|\mathbf{x}^s\|_2. \end{aligned}$$

(b) Finally, we bound the second term on the right hand side of Eqn. 30 as follows.

$$\begin{aligned} \|\mathbf{a}_{B^{[n+1]}}^{[n+1]} - \mathbf{x}_{B^{[n+1]}}^s\|_2 &= \|\hat{\mathbf{x}}_{B^{[n+1]}}^{[n]} + \mu^{[n]}\Phi_{B^{[n+1]}}^T (\mathbf{y} - \Phi\hat{\mathbf{x}}^{[n]}) - \mathbf{x}_{B^{[n+1]}}^s\|_2 \\ &= \|\hat{\mathbf{x}}_{B^{[n+1]}}^{[n]} + \mu^{[n]}\Phi_{B^{[n+1]}}^T (\Phi\mathbf{x}^s + \epsilon - \Phi\hat{\mathbf{x}}^{[n]}) - \mathbf{x}_{B^{[n+1]}}^s\|_2 \\ &= \|\mathbf{r}_{B^{[n+1]}}^{[n]} - \mu^{[n]}\Phi_{B^{[n+1]}}^T (\Phi\mathbf{r}^{[n]} - \epsilon)\|_2 \\ &= \|\mathbf{r}_{B^{[n+1]}}^{[n]} - \mu^{[n]}\Phi_{B^{[n+1]}}^T (\Phi_{B^{[n+1]}}\mathbf{r}_{B^{[n+1]}}^{[n]} + \Phi_{B^{[n]}\setminus B^{[n+1]}}\mathbf{r}_{B^{[n]}\setminus B^{[n+1]}}^{[n]} - \epsilon)\|_2 \\ &\leq \|(\mathbf{I} - \mu^{[n]}\Phi_{B^{[n+1]}}^T \Phi_{B^{[n+1]}})\mathbf{r}_{B^{[n+1]}}^{[n]}\|_2 \\ &\quad + \|\mu^{[n]}\Phi_{B^{[n+1]}}^T \Phi_{B^{[n]}\setminus B^{[n+1]}}\mathbf{r}_{B^{[n]}\setminus B^{[n+1]}}^{[n]}\|_2 \\ &\quad + \|\mu^{[n]}\Phi_{B^{[n+1]}}^T \epsilon\|_2. \end{aligned} \quad (41)$$

It can easily be verified that

$$\begin{aligned} \|(\mathbf{I} - \mu^{[n]}\Phi_{B^{[n+1]}}^T \Phi_{B^{[n+1]}})\mathbf{r}_{B^{[n+1]}}^{[n]}\|_2 &\stackrel{(1)}{\leq} \gamma_{2s}\|\mathbf{r}_{B^{[n+1]}}^{[n]}\|_2 \\ \|\mu^{[n]}\Phi_{B^{[n+1]}}^T \Phi_{B^{[n]}\setminus B^{[n+1]}}\mathbf{r}_{B^{[n]}\setminus B^{[n+1]}}^{[n]}\|_2 &\leq (\|\mu^{[n]}\Phi_{\Gamma_1}^T \Phi_{B^{[n]}\setminus B^{[n+1]}}\mathbf{r}_{B^{[n]}\setminus B^{[n+1]}}^{[n]}\|_2^2 \\ &\quad + \|\mu^{[n]}\Phi_{\Gamma_2}^T \Phi_{B^{[n]}\setminus B^{[n+1]}}\mathbf{r}_{B^{[n]}\setminus B^{[n+1]}}^{[n]}\|_2^2)^{1/2} \\ &\stackrel{(2)}{\leq} \sqrt{2}\gamma_{2s}\|\mathbf{r}_{B^{[n]}\setminus B^{[n+1]}}^{[n]}\|_2 \\ \|\mu^{[n]}\Phi_{B^{[n+1]}}^T \epsilon\|_2 &\stackrel{(3)}{\leq} \frac{\gamma_{2s} + 1}{\beta_{2s}} \|\epsilon\|_2 + \sqrt{2}(\gamma_{2s} + 1) [\|\mathbf{x} - \mathbf{x}^s\|_2 - \frac{\|\mathbf{x} - \mathbf{x}^s\|_1}{\sqrt{s}}] \end{aligned} \quad (42)$$

where (1) and (2) follow from Lemma ??, (3) is derived in 37.

(b) By the orthogonality between  $\mathbf{r}_{B^{[n+1]}}^{[n]}$  and  $\mathbf{r}_{B^{[n]} \setminus B^{[n+1]}}^{[n]}$ , Eqn.41 can further be simplified to

$$\|\mathbf{a}_{B^{[n+1]}}^{[n+1]} - \mathbf{x}_{B^{[n+1]}}^s\|_2 \|\mathbf{x}^{[n]}\|_2 \leq 2\gamma_{2s} \|\mathbf{r}^{[n]}\|_2 + \frac{\gamma_{2s} + 1}{\beta_{2s}} \|\mathbf{e}\|_2 + \sqrt{2}(\gamma_{2s} + 1) \left[ \|\mathbf{x} - \mathbf{x}^s\|_2 - \frac{\|\mathbf{x} - \mathbf{x}^s\|_1}{\sqrt{s}} \right]. \quad (43)$$

Substituting Eqn.35,38,39,40 and 43 into Eqn.29, the norm of recovery error is given by

$$\begin{aligned} \mathbb{E}[\|\mathbf{r}^{[n+1]}\|_2 \|\mathbf{r}^{[n]}\|_2] &\leq 8 \max(\gamma_{2s}, \hat{\gamma}_{2s}) \|\mathbf{r}^{[n]}\|_2 + 4 \max\left(\frac{(1 + \gamma_{2s})}{\beta_{2s}}, \frac{(1 + \hat{\gamma}_{2s})}{\hat{\beta}_{2s}}\right) \|\mathbf{e}\|_2 \\ &\quad + 2\sqrt{2}(2 \max(\gamma_{2s}, \hat{\gamma}_{2s}) + 1) \left[ \|\mathbf{x} - \mathbf{x}^s\|_2 + \frac{\|\mathbf{x} - \mathbf{x}^s\|_1}{\sqrt{s}} \right] \\ &\quad + 2 \frac{(1 + \hat{\gamma}_{2s})\sqrt{M}}{\hat{\beta}_{2s}} \left( \frac{c_{\Phi} \|\mathbf{x}^s\|_2}{2^{b_{\Phi}-1}} + \frac{c_{\mathbf{y}}}{2^{b_{\mathbf{y}}-1}} \right) \end{aligned} \quad (44)$$

Let  $\gamma_{2s}, \hat{\gamma}_{2s} \leq t$ . For  $t \leq 1/16$ , we have

$$\mathbb{E}[\|\hat{\mathbf{x}}^{[n+1]} - \mathbf{x}^s\|_2 \|\hat{\mathbf{x}}^{[0]} = \mathbf{0}\|] \leq 2^{-n} \|\mathbf{x}^s\|_2 + 10\|\mathbf{e}\|_2 + 6.4 \left[ \|\mathbf{x} - \mathbf{x}^s\|_2 + \frac{\|\mathbf{x} - \mathbf{x}^s\|_1}{\sqrt{s}} \right] + \frac{5\sqrt{M}}{\hat{\beta}_{2s}} \left( \frac{c_{\Phi} \|\mathbf{x}^s\|_2}{2^{b_{\Phi}-1}} + \frac{c_{\mathbf{y}}}{2^{b_{\mathbf{y}}-1}} \right) \quad (45)$$

and using the following notation:

$$\begin{aligned} \epsilon_s &:= \|\mathbf{x} - \mathbf{x}^s\|_2 + \frac{\|\mathbf{x} - \mathbf{x}^s\|_1}{\sqrt{s}} + \frac{1}{\beta_{2s}} \|\mathbf{e}\|_2 \\ \epsilon_q &:= \frac{\sqrt{M}}{\hat{\beta}_{2s}} \left( \frac{c_{\Phi} \|\mathbf{x}^s\|_2}{2^{b_{\Phi}-1}} + \frac{c_{\mathbf{y}}}{2^{b_{\mathbf{y}}-1}} \right) \end{aligned} \quad (46)$$

we finally have

$$\mathbb{E}[\|\hat{\mathbf{x}}^{[n+1]} - \mathbf{x}^s\|_2 \|\hat{\mathbf{x}}^{[0]} = \mathbf{0}\|] \leq 2^{-n} \|\mathbf{x}^s\|_2 + 10\epsilon_s + 5\epsilon_q. \quad (47)$$

### 6.3. Proof of Lemma 1

Assume that  $\Phi_{\Gamma}$  has the singular values confined in  $[\alpha_{|\Gamma|}, \beta_{|\Gamma|}]$ . In [39, 40, 42], the perturbation of singular values of a matrix upon corruption of entries with noise is heavily studied. Moreover, it is shown that Bernoulli noise, corrupting the entries of the matrix independently, lifts up the singular values of the matrix, and at most by  $\sigma_{\max} \sqrt{|\Gamma|}$  where  $\sigma_{\max}$  is the maximum of the noise standard deviations. Therefore, singular values of  $\hat{\Phi}_{\Gamma}$  is in  $[\alpha_{|\Gamma|}, \beta_{|\Gamma|} + \sigma_{\max} \sqrt{|\Gamma|}]$ . Moreover, we previously showed that the variance of the quantization noise is at most  $1/2^{b-1}$ , hence we have  $\sigma_{\max} = 1/2^{b-1}$ . Hence,  $\hat{\gamma}_{|\Gamma|}$  satisfies

$$\hat{\gamma}_{|\Gamma|} \leq \gamma_{|\Gamma|} + \frac{\sqrt{|\Gamma|}}{2^{b-1} \alpha_{|\Gamma|}}. \quad (48)$$

The above equation guarantees that whenever  $\gamma_{|\Gamma|} + \epsilon \leq 1/16$ , for some  $\epsilon \geq \frac{\sqrt{|\Gamma|}}{2^{b-1} \alpha_{|\Gamma|}}$ ,  $\hat{\gamma}_{|\Gamma|}$  is guaranteed to be lower than  $1/16$ .

## 7. Radio Interferometer Pipeline

Antennas at various locations on the ground records radio waves coming from the sources in space, and then send those to *interferometers* (correlator unit), which first estimate correlation between the time series-measurements so-called visibilities. Then the central processor estimates the sky image with a specified imaging technique, i.e., CLEAN [24] and A(W)-projection [4].

### 7.1. Basic Data Model

Let us start with the following modeling assumptions: [41]

1. Celestial sources are in far field, the series emanating from sources and captured by the antennas are thus paralel,
2. series emitted by celestial sources are narrow band zero mean circularly-symmetric complex Gaussian processes,
3. series originating from different directions in the sky are uncorrelated.

(1) follows from the assumption sources lie on a hypothetical sphere, the so-called celestial sphere. This implies that we can not measure how far the sources are.

Let  $\hat{s}(t, \mathbf{r})$  denote the series emitted by the source coming from the direction  $\mathbf{r} \in \mathbb{S}^2$ . (2), therefore, implies  $\hat{s}(t, \mathbf{r}) \sim \mathcal{CN}(0, I(\mathbf{r}))$  where  $I(\mathbf{r})$  is the intensity of the source series emanating from direction  $\mathbf{r}$ . Given the center frequency  $f_0 \in \mathbb{R}$ , (2) yields the following baseband representation of  $\hat{s}(t, \mathbf{r})$ :

$$s(t, \mathbf{r}) = \hat{s}(t, \mathbf{r})e^{j2\pi f_0 t}. \quad (49)$$

Note also that  $\mathbb{E}[s(t, \mathbf{r}_1)s^*(t, \mathbf{r}_2)] = 0, \forall \mathbf{r}_1, \mathbf{r}_2 \in \mathbb{S}^2$  follows from (3), where  $*$  denotes the conjugate operator. The series coming from direction  $\mathbf{r}$  and recorded by antenna  $i$  is thus given by:

$$x_i(t, \mathbf{r}) = s(t - \tau_i(\mathbf{r}), \mathbf{r}) \quad (50)$$

where  $\tau_i(\mathbf{r})$  denotes the time delay for the series reaching from the source to reach at the antenna  $i$ . Combining Eqn. 49 and 50 we have

$$x_i(t, \mathbf{r}) = \hat{s}(t - \tau_i(\mathbf{r}), \mathbf{r})e^{j2\pi f_0(t - \tau_i(\mathbf{r}))}. \quad (51)$$

The above derivations concern merely a specific source. Let now focus on the series measured by the antenna  $i$  coming from multiple sources (from all directions). It is then by the following integral:

$$x_i(t) = \iint_{\mathbb{S}^2} \hat{s}(t - \tau_i(\mathbf{r}), \mathbf{r})e^{j2\pi f_0(t - \tau_i(\mathbf{r}))} d\mathbf{r}. \quad (52)$$

As correlations between the antenna time-series are of special interest of imaging, let us have a closer look at the algebraic equations regarding the correlations. Recall that the source series coming from different directions in space are uncorrelated. Using this, we have the following closed-form expression:

$$\mathbb{E}[x_i(t)x_k(t)^*] = \iint_{\mathbb{S}^2} \mathbb{E}[\hat{s}(t - \tau_i(\mathbf{r}), \mathbf{r})\hat{s}^*(t - \tau_k(\mathbf{r}), \mathbf{r})]e^{-j2\pi f_0(\tau_i(\mathbf{r}) - \tau_k(\mathbf{r}))} d\mathbf{r} \quad (53)$$

where  $i$  and  $k$  denote different antennas. By the assumption of (2), the series  $\hat{s}(t, \mathbf{r})$  remains constant over the time shift we further have

$$\mathbb{E}[x_i(t)x_k(t)^*] = \oint_{\mathbb{S}^2} I(\mathbf{r})e^{-j2\pi f_0(\tau_i(\mathbf{r})-\tau_k(\mathbf{r}))} d\mathbf{r} \quad (54)$$

where  $I(\mathbf{r})$  denotes the variance of the series emitted from direction  $\mathbf{r}$  referblack to as sky image. We further have

$$\tau_i(\mathbf{r}) = \frac{1}{c}\langle \mathbf{r}_{\text{norm}}, \mathbf{p}_i \rangle \quad (55)$$

where  $\mathbf{r}_{\text{norm}} = \frac{\mathbf{r}}{\|\mathbf{r}\|_2}$  and  $\mathbf{p}_i$  denotes the position of antenna  $i$ . The above relation together with Eqn. 54 gives us that

$$\mathbb{E}[x_i(t)x_k(t)^*] = \oint_{\mathbb{S}^2} I(\mathbf{r})e^{-j2\pi \frac{f_0}{c}\langle \mathbf{r}_{\text{norm}}, \mathbf{p}_i - \mathbf{p}_k \rangle} d\mathbf{r}. \quad (56)$$

Note that  $\frac{f_0}{c} = \frac{1}{\lambda_0}$  where  $\lambda_0$  is the wavelength of the observation, Eqn. 56 can be further simplified to the following equation:

$$\mathbb{E}[x_i(t)x_k(t)^*] = \oint_{\mathbb{S}^2} I(\mathbf{r})e^{-j2\pi\langle \mathbf{r}_{\text{norm}}, \frac{\mathbf{p}_i - \mathbf{p}_k}{\lambda_0} \rangle} d\mathbf{r}. \quad (57)$$

Consider now a specific region of interest centered around  $\mathbf{r}_0$  and basis vectors  $\hat{\mathbf{e}}_1$ ,  $\hat{\mathbf{e}}_2$  and  $\hat{\mathbf{e}}_3$  where  $\hat{\mathbf{e}}_1$  points in the direction of rotation of the earth,  $\hat{\mathbf{e}}_3$  denotes the direction of  $\mathbf{r}_0$  and  $\hat{\mathbf{e}}_2$  is perpendicular to  $\hat{\mathbf{e}}_1$  and  $\hat{\mathbf{e}}_3$ .  $\mathbf{r}$  can be therefore approximated to  $r \approx l\hat{\mathbf{e}}_1 + m\hat{\mathbf{e}}_2 + 1\hat{\mathbf{e}}_3$ <sup>1</sup>. Similarly,  $\frac{\mathbf{p}_i - \mathbf{p}_k}{\lambda_0}$  can also be expressed in terms of the basis vectors, i.e.,  $\frac{\mathbf{p}_i - \mathbf{p}_k}{\lambda_0} = u_{i,k}\hat{\mathbf{e}}_1 + v_{i,k}\hat{\mathbf{e}}_2 + w_{i,k}\hat{\mathbf{e}}_3$ . Substituting these into Eqn. 57, we get

$$\mathbb{E}[x_i(t)x_k^*(t)] = \iint_{K \subset \mathbb{R}^2} \frac{e^{-j2\pi w_{i,k}(\sqrt{1-l^2-m^2}-1)}}{\sqrt{1-l^2-m^2}} I(l, m)e^{-j2\pi(u_{i,k}l+v_{i,k}m)} dl dm \quad (58)$$

where  $K$  is the compact support of  $I \in \mathbb{R}^2$ .

As indicated earlier, the field of view is small pointing  $\mathbf{r}_0$ , i.e., small  $l$  and  $m$ . Hence  $\frac{e^{-j2\pi w_{i,k}}}{\sqrt{1-l^2-m^2}-1} \sim 1$  and  $\sqrt{1-l^2-m^2}$  term can be assumed to be constant. The above resulting representation can then be further simplified to the following:

$$\mathbb{E}[x_i(t)x_k^*(t)] = \iint_{K \subset \mathbb{R}^2} e^{-j2\pi w_{i,k}} I(l, m)e^{-j2\pi(u_{i,k}l+v_{i,k}m)} dldm. \quad (59)$$

**Key definition:** The *visibility* function is defined by removing the constant phase  $e^{-j2\pi w_{i,k}}$  as follows:

$$V(u, v) \stackrel{\text{def}}{=} \iint_{K \subset \mathbb{R}^2} I(l, m)e^{-j2\pi(ul+vm)} dldm. \quad (60)$$

<sup>1</sup>More clearly;  $(\mathbf{r} - \mathbf{r}_0) + \mathbf{r}_0 \approx l\hat{\mathbf{e}}_1 + m\hat{\mathbf{e}}_2 + 1\hat{\mathbf{e}}_3$ .

Therefore, each sample of this function is given by  $V(u_{i,k}, v_{i,k}) = \mathbb{E}[x_i(t)x_k^*(t)]$ .

Remark that *visibility* equation is an integration of the product of sky intensity and a complex exponential over the unit sphere, which can be represented as a two dimensional Fourier transform. Therefore, this function is equivalent to Fourier transform of the image  $I(l, m)$ . This relation is known as van Cittert-Zernike theorem [41]. Consequently, the samples of  $V(u, v)$  are sufficient for sky image recovery where each baseline gives an approximate sample from Fourier transform of the sky image. This can be mathematically stated as follows:

$$V_{i,k} \sim V(u_{i,k}, v_{i,k}) = \iint_{K \subset \mathbb{R}^2} I(l, m) e^{-j2\pi(u_{i,k}l + v_{i,k}m)} dl dm. \quad (61)$$

Therefore, the sky image can be recovered by taking inverse Fourier transform of the non-uniformly sampled visibility function so-called *dirty image* as follows:

$$I_d(l, m) = \mathcal{F}^{-1} \left\{ \sum_{i,k} V(u, v) \delta(u - u_{i,k}, v - v_{i,k}) \right\}. \quad (62)$$

A closer look into the above equation reveals that *dirty image* is equivalent to

$$I_d(l, m) = I(l, m) * I_{db}(l, m) \quad (63)$$

where

$$I_{db}(l, m) = \sum_{i,k} e^{j2\pi(u_{i,k}l + v_{i,k}m)} \quad (64)$$

is called *dirty beam* with  $k$  baselines (( $i, k$ ) pairs with the previous notation),  $I(l, m)$  is the true sky map, and  $*$  denotes convolution operator.

The imaging problem in radio astronomy can be viewed as reconstructing a sky image from estimates of its Fourier transform samples. Moreover, the problem is ill-posed as we have finite number of antennas thus the baselines. This can be tackled with up to some level by introducing a prior sky model. After having reviewed the basic data model and revealed how visibilities link to Fourier transform of the sky intensities, let us now focus on the data model from array series processing point of view.

As widely used, we (very often astronomers as well) assume a point source model for the sky [2, 41]. The series measured by the antenna  $i$  denoted by  $x_i(t)$  is given by:

$$x_i(t) = \sum_{q=1}^Q \hat{s}(t - \tau_{i,q}, \mathbf{r}_q) e^{j2\pi f_0(t - \tau_{i,q})} \quad (65)$$

where  $\tau_{i,q}$  is the time delay at the antenna  $i$  for source  $q$  and  $Q$  denotes the number of sources.

Recall that the series  $\hat{s}(t, r)$  remains constant over the time shift, i.e.,  $\hat{s}(t - \tau_{i,q}, \mathbf{r}_q) =$

$\hat{s}(t - \tau_{k,q}, \mathbf{r}_q)$ ,  $\forall i, k$  and hence Eqn. 65 can be simplified as follows:

$$\begin{aligned} x_i(t) &\stackrel{(1)}{=} \sum_{q=1}^Q \hat{s}(t - \tau_{i,q}, \mathbf{r}_q) e^{j2\pi f_0(t - \tau_{i,q})} \\ &\stackrel{(2)}{=} \sum_{q=1}^Q \hat{s}(t, \mathbf{r}_q) e^{j2\pi f_0(t - \tau_{i,q})} \\ &\stackrel{(3)}{=} \sum_{q=1}^Q \hat{s}_q(t) e^{j2\pi f_0(t - \tau_{i,q})} \end{aligned} \quad (66)$$

where (1) and (2) follow from the arguments above. To simplify notation, we denote  $\hat{s}(t, \mathbf{r}_q)$  by  $\hat{s}_q(t)$  which leads (3). By Eqn. 55, we have

$$x_i(t) = \sum_{q=1}^Q \hat{s}_q(t) e^{j2\pi f_0(t - \langle \mathbf{r}_q, \lambda_0 \mathbf{p}_i \rangle / c)}. \quad (67)$$

Consider now that antenna series  $x_i(t)$ ,  $i \in \{1, \dots, L\}$  are concatenated in a vector  $\mathbf{x}(t) \in \mathbb{C}^L$ . Eqn. 67 can be re-written as

$$\mathbf{x}(t) = e^{j2\pi f_0 t} \sum_{q=1}^Q \mathbf{a}_q \hat{s}_q(t) \quad (68)$$

where  $\mathbf{a}_q \in \mathbb{C}^L$  so-called *antenna steering vector* is given by

$$\mathbf{a}_q = \begin{bmatrix} e^{-j2\pi \langle \mathbf{r}_q, \mathbf{p}_1 \rangle} \\ e^{-j2\pi \langle \mathbf{r}_q, \mathbf{p}_2 \rangle} \\ \vdots \\ e^{-j2\pi \langle \mathbf{r}_q, \mathbf{p}_L \rangle} \end{bmatrix} \quad (69)$$

towards source  $q$ .

Let  $\mathbf{A} \in \mathbb{C}^{L \times Q}$  denote *antenna steering matrix* with each column given by individual *antenna steering vector*  $\mathbf{a}_q$  and also  $\hat{\mathbf{s}}(t)$  be vector of source series  $\hat{s}_q(t)$ ,  $q \in \{1, 2, \dots, Q\}$ . We then have following matrix product:

$$\mathbf{x}(t) = e^{j2\pi f_0 t} \mathbf{A} \hat{\mathbf{s}}(t). \quad (70)$$

Up to now, we have introduced the data model under perfect conditions in means of noise. Real-life scenarios however are not that optimistic. Conversely, thermal noise usually has a big share in the series measurablack by the antennas. Let thus  $\mathbf{n}(t) \in \mathbb{C}^L$  be the additive white Gaussian noise (AWGN) at the antennas. More realistic model for  $\mathbf{x}(t)$  in presence of noise can be as the following:

$$\mathbf{x}(t) = e^{j2\pi f_0 t} \mathbf{A} \hat{\mathbf{s}}(t) + \mathbf{n}(t) \quad (71)$$

where  $\mathbf{n}(t)$  is assumed to be independently drawn from the distribution  $\mathbb{CN}(0, \sigma_n^2 \mathbf{I}_L)$ ,  $\sigma_n \in \mathbb{R}$  and  $\mathbf{I}_L$  is  $L \times L$  identity matrix. Moreover, the series emitted by the sources  $\hat{\mathbf{s}}(t)$  are also modelled as stochastic processes where the parameters to be estimated, i.e.,  $\hat{\mathbf{s}}(t) \sim \mathbb{CN}(0, \mathbf{\Sigma}_s)$  where  $\mathbf{\Sigma}_s$  is the diagonal covariance matrix for the source series  $\hat{\mathbf{s}}(t)$ .

Let  $\mathbf{V}$  account for the visibility (cross-correlation) matrix. Then

$$\begin{aligned} \mathbf{V} &= \mathbb{E}[\mathbf{x}(t)\mathbf{x}^\dagger(t)] \\ &= \mathbb{E}[(e^{j2\pi f_0 t} \mathbf{A} \hat{\mathbf{s}}(t))(e^{j2\pi f_0 t} \mathbf{A} \hat{\mathbf{s}}(t))^\dagger] \\ &= \mathbf{A} \mathbf{\Sigma}_s \mathbf{A}^\dagger + \mathbf{\Sigma}_n. \end{aligned} \quad (72)$$

### 7.2. Formation of $\Phi$

We first form a grid of sky map by  $\mathbf{I}_{l,m} \in \mathbb{R}^{r \times r}$  for  $l, m \in \{1, 2, \dots, r\}$ , where  $r$  is the resolution of the map. Let  $\mathbf{p}_{i,k} \in \mathbb{R}^2$  denote the two-dimensional distance between  $i$ 'th and  $k$ 'th antenna, and  $\mathbf{r}_{l,m} \in \mathbb{R}^2$  stand for two-dimensional position of pixel in  $l$ 'th row and  $m$ 'th column of  $\mathbf{I}$ , respectively.

Using Eqn. 61, we can approximate the noisy visibilities by

$$\mathbf{V}_{i,k} = \sum_{l,m} \mathbf{I}_{l,m} e^{-j2\pi f_0 \langle \mathbf{p}_{i,k}, \mathbf{r}_{l,m} \rangle} + \delta_{i,k}. \quad (73)$$

**Definition 1.** Let  $\mathbf{A} \in \mathbb{K}^{M \times N}$  be a matrix, with field  $\mathbb{K}$ . The  $\text{vec}(\cdot)$  operator is defined

$$\text{vec}(\cdot) : \mathbb{K}^{M \times N} \rightarrow \mathbb{K}^{MN}.$$

Using above definition we can reformulate Eqn. 73 as follows.

$$\mathbf{y} = \Phi \mathbf{x} + \mathbf{e} \quad (74)$$

with  $\mathbf{y}, \mathbf{e} \in \mathbb{C}^M$ ,  $\Phi \in \mathbb{C}^{M \times N}$  and  $\mathbf{x} \in \mathbb{R}^N$  such that  $\mathbf{y} = \text{vec}(\mathbf{V})$ ,  $\mathbf{x} = \text{vec}(\mathbf{I})$ ,  $\mathbf{e} = \text{vec}(\mathbf{\Sigma}_n)$  and finally

$$\Phi_{z,w} = e^{-j2\pi f_0 \langle \mathbf{p}_{i,k}, \mathbf{r}_{l,m} \rangle} \quad (75)$$

where  $z = i + L(k - 1)$ ,  $i, k = \{1, 2, \dots, L\}$  and  $w = l + r(m - 1)$ ,  $l, m = \{1, 2, \dots, r\}$ .

### 7.3. How we satisfy conditions on Restricted Isometry Property?

Real-life problems usually lack of traditional RIP, that is,  $\|\Phi\|_2 < 1$ . The scale-invariant feature of the measurement matrix used in normalized IHT however alleviates the RIP condition and imposes a fairly mild constraint in Eqn. 17, i.e., non-symmetric RIP. In a series of paper [10, 11], CoSaMP is shown to perform markedly worse when the RIP condition fails. IHT, however, still preserves its near-optimal recoveries far beyond the region of RIP. Recall from the main paper that the step size  $\hat{\mu}^{[n]}$  is required to counteract the scaling of  $\hat{\Phi}$  such that  $\|\hat{\mu}^{0.5} \hat{\Phi}\|_2^2 < 1$  to ensure the convergence.



The adaptive step size setting of normalized IHT yields the trivial bound on  $\mu$  as [11]

$$1/\hat{\beta}_{2s}^2 \leq 1/\hat{\beta}_s^2 < \hat{\mu}^{[n]} < 1/\hat{\alpha}_s^2 \leq 1/\hat{\alpha}_{2s}^2. \quad (76)$$

Convergence is trivial in low precision setting provided that  $\hat{\mu}^{[n]}$  is chosen adaptively according to the above strategy. Regarding performance guarantees, however, in Theorem 3 we show that if  $\gamma_{2s} = \beta_{2s}/\alpha_{2s} - 1, \hat{\gamma}_{2s} = \hat{\beta}_{2s}/\hat{\alpha}_{2s} - 1 \leq 1/16$ , then the recovery error inversely scales with  $\beta_{2s}$  and  $\hat{\beta}_{2s}$ , which we can up-scale hence reduce the error. We previously sketch the values of  $\beta_{2s}$  and  $\hat{\beta}_{2s}$  for the current setting in our paper and show that they are large enough to diminish recovery error and no upscale is necessity in radio astronomy case. Yet, for provable guarantees, yet, we need to satisfy the conditions on  $\gamma_{2s}$  and  $\hat{\gamma}_{2s}$ . Clearly, this cannot be done by re-scaling  $\beta_{2s}$  and  $\hat{\beta}_{2s}$  because  $\alpha_{2s}$  and  $\hat{\alpha}_{2s}$  will be scaled accordingly. Luckily, in certain applications, instrument dependent parameters can enable the adjustment of the RIP condition such that  $\gamma_{2s}, \hat{\gamma}_{2s} \leq 1/16$ . For example, in radio astronomy, we have the flexibility to ensure the conditions on  $\gamma_{2s}$  and  $\hat{\gamma}_{2s}$  holds as follows.

Let us form a grid on  $[l, m]$ ,  $l, m \in [-d, d]$  where the sky map is displayed. By changing  $d$ , we change the measurement matrix and hence the bounds on  $\gamma_{2s}$  hence  $\hat{\gamma}_{2s}$  can be tuned. Moreover, given the set of antennas, we can pick the best order of antennas as well as suitable number of antennas that ensures the desired condition. Fig 7 and 8 illustrate the numerical experiments conducted in the current setting where we recover the sky map with resolution of 256 pixels per axis. The numerical results suggest that these conditions in the certain settings and can be further refined with parameter  $d$  and number of antennas. In Fig 7, we illustrate the RIP condition for the measurement matrix  $\Phi$ . We also evaluate the number of bits required to ensure RIP condition of quantized measurement matrix. That is, we can reduce the precision down to 2 bits per value. The number of antennas used in this setting is 30.

In Fig. 8, however, we illustrate the effect of number of antennas on the RIP condition of measurement matrix. The number of bits to represent data points can be picked accordingly to ensure RIP condition. We illustrate this in Fig. 7, same applies to Fig. 8.

#### 7.4. Performance Analysis with NIHT

In radio astronomy application, the recovery error of NIHT can be simplified as follows. The point source assumption implies that the signal is naturally sparse such that  $\mathbf{x} = \mathbf{x}^s$ . Let also  $\sigma_n^2$  is the variance of noise corrupting antennas. Referring to Section 7, we have  $\|\mathbf{e}\|_2 = \sqrt{L}\sigma_n$ . Hence if  $\gamma_{2s}, \hat{\gamma}_{2s} \leq 1/16$ , substituting these into Eqn. 47, low precision IHT recovers  $\mathbf{x}$  with accuracy

$$\mathbb{E}[\|\mathbf{x}^{n+1} - \mathbf{x}^s\|_2] \leq 2^{-n}\|\mathbf{x}^s\|_2 + 9\frac{\sqrt{L}}{\beta_{2s}}\sigma_n + 5\frac{L}{\hat{\beta}_{2s}}\epsilon_{\text{sky}}. \quad (77)$$

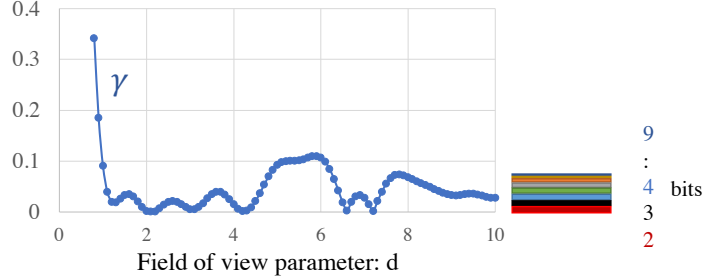


FIG 7.  $\gamma$  here is defined as  $\max \sigma_i / \min \sigma_i - 1$  where  $\sigma_i$  is the singular values of full measurement matrix. Remark that,  $\gamma \leq 1/16$  ensures that  $\gamma_{|\Gamma|} \leq 1/16$  for any support subset  $\Gamma$ .  $\gamma$  can be tuned by an instrument dependent parameter  $d$ . Using Lemma 1, we evaluate minimum number of bits to ensure that  $\hat{\Phi} \leq 1/16$  for each  $d$  and hence its respective  $\Phi$ . The figure suggests that we can reduce the precision of  $\Phi$  down to 2 bits if  $\Phi$  is properly designed. Ensuring that  $\hat{\Phi} \leq 1/16$ ,  $\hat{\Phi}_{|\Gamma|} \leq 1/16$  over any  $\Gamma$  is guaranteed. That is, the quantized measurement matrix also satisfies non-symmetric RIP.

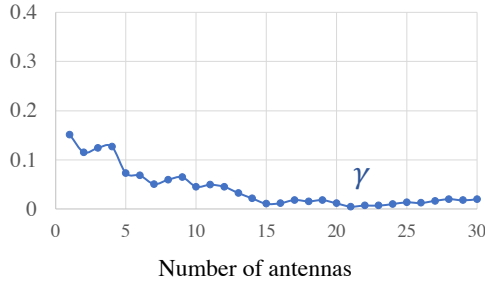


FIG 8.  $\gamma$  values for different number of antennas used for imaging. Employing more antennas, RIP condition on the full precision measurement matrix can be satisfied. Similarly, by using Lemma 1 in the main body, we can evaluate the number of bits to quantize measurement matrix in advance.

### 7.5. Inverse Fourier transform combined with CLEAN algorithm

Referring to Eqn. 63 & 64, current imaging techniques first performs naive inverse Fourier transform of the visibilities such that

$$\mathbf{I}_d(l, m) = \sum_{i,j} V(u_{i,j}, v_{i,j}) e^{j2\pi(u_{i,j}l + v_{i,j}m)}. \quad (78)$$

Location and flux intensities of the sources are estimated by the CLEAN algorithm.

CLEAN algorithm (a deconvolution algorithm) therefore takes the *dirty image*  $\mathbf{I}_d(l, m)$  as input and outputs a sparse sky map by iteratively removing a fraction<sup>2</sup> of the highest peak convolved with the *dirty beam*  $\mathbf{I}_{db}(l, m)$ . The algorithmic steps for full sky imaging is summarized in Algorithm 2.

<sup>2</sup>so-called *loop gain*  $\leq 0.3$

---

**Algorithm 2** The CLEAN algorithm for basic data model
 

---

**Input:** Dirty image:  $\mathbf{I}_d(\mathbf{r})$ , Dirty beam:  $\mathbf{I}_{db}(\mathbf{r})$ , loop gain:  $\lambda$ , a stopping threshold  $v$ 
**Output:** CLEAN component list: flux and location of point sources

**repeat**

 Initialize the residual map  $\hat{\mathbf{I}}(\mathbf{r})$  to  $\mathbf{I}_d(\mathbf{r})$ 
**for**  $n = 1$  **to**  $n^*$  **do**

 Find the location maximum peak of  $\hat{\mathbf{I}}(\mathbf{r})$ :  $\mathbf{r}_p$ 

 Update the residual map:  $\hat{\mathbf{I}}(\mathbf{r}) \leftarrow \hat{\mathbf{I}}(\mathbf{r}) - \lambda \hat{\mathbf{I}}(\mathbf{r}_p) \mathbf{I}(\mathbf{r} - \mathbf{r}_p)$ 

 Add  $\mathbf{r}_p$  and  $\hat{\mathbf{I}}(\mathbf{r}_p)$  to the CLEAN component list

**end for**
**until**  $\max \hat{\mathbf{I}} < v$ 


---

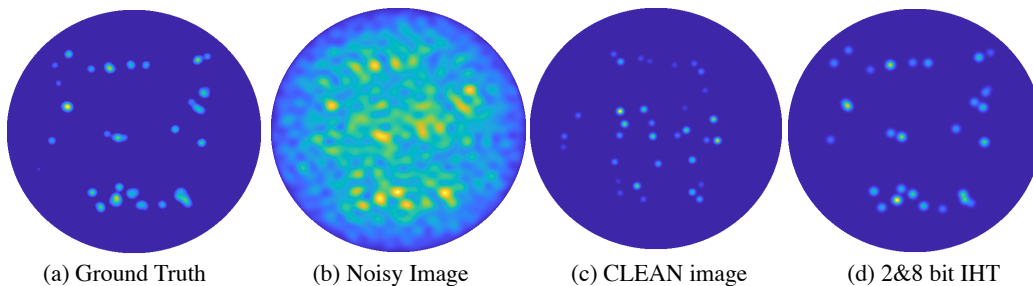


FIG 9. Comparison of 2&8 bit IHT to CLEAN Algorithm. The CLEAN mostly captures the noise artefacts as actual sources unlike IHT.

Recall from the discussions in the main paper that noise in receivers is far stronger than the weak incoming signals thus low SNR at the antenna level results, i.e., usually ranged from -5 to 5 dB. In Fig. 9, we apply the CLEAN algorithm to the LOFAR data set we use throughout the main paper, where SNR is computed nearly 0 dB. This particular experiment states that the CLEAN algorithm notably underperforms in the presence of significant noise. This undesirable property is yet not surprising. A careful look into the the algorithmic steps, it apparently matches also to the noise artefacts in the image considering them as a point source. This can also be justified mathematically: we designed the problem such that an execution of CLEAN corresponds to the first iteration recovery of IHT, which interprets our numerical results.

Computationally, the CLEAN requires a 2D Fourier inversion and deconvolution per iteration thus the operational expense of the method is relatively higher compared to those of IHT and CoSaMP.

## 8. FPGA Implementation Details

Field-Programmable Gate Arrays (FPGA) are an alternative to commonly used Graphics Processing Units (GPU) for accelerated processing of compute intensive machine learning workloads. The custom logic fabric of an FPGA enables the design of specialized compute

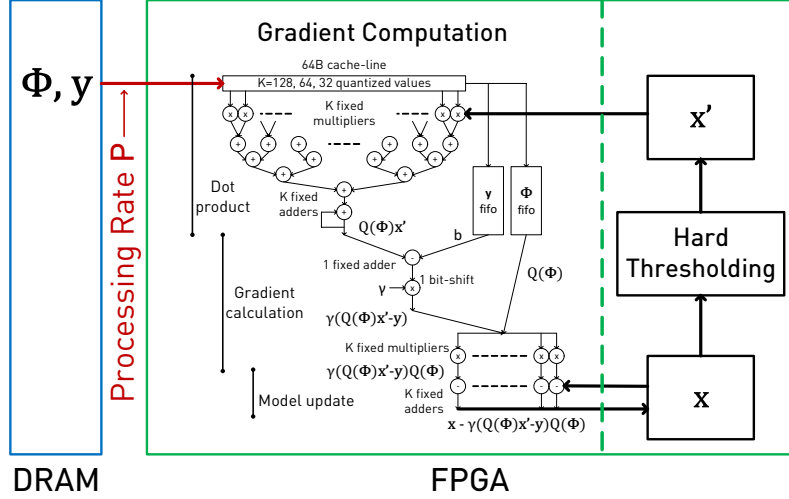


FIG 10. IHT on an FPGA-based system.

units, which is very advantageous when working on extremely low-precision and irregular numeric formats, such as 2 bit numbers. Thanks to the microarchitectural flexibility advantage, it is possible to achieve near linear speed-up when lowering the precision of data that is read from the memory. This has been shown recently for stochastic gradient descent (SGD) when training linear models [48, 28]. In this work, we use the open-source FPGA implementation from the mentioned works and modify it to perform IHT.

In terms of the computation, we need to modify two parts of the design to convert it from performing SGD to IHT: 1) Instead of updating the model after a mini-batch count is reached, we update it after all samples are processed and the true gradient is available. 2) After each epoch, we perform a binary search on the updated model to find the threshold value satisfying that only top  $S$  values are larger than the threshold.

### 8.1. Performance analysis

The gradient computation unit as shown in Fig. 10 reads the measurement matrix  $\Phi$  and the measurements  $y$  from main memory and keeps  $x$  in on-chip memory. We note that transferring  $\Phi$  from main memory will be necessary in most practical settings, where the matrix  $\Phi$  is too large to fit onto the FPGA. The FPGA is able to process data from memory at a rate of  $P = 12.8 \text{ GB/s}$ . Thus, performance will be bound on this rate  $P$  for processing  $\Phi$  and  $y$ , which becomes the system bottleneck. The time for each iteration is given by  $T = \text{size}(\Phi)/P$ , since  $\text{size}(y) \ll \text{size}(\Phi)$ . We can achieve significant speed-up by quantizing  $\Phi$ , simply because we reduce the amount of data to be transferred: more entries arrive with each transfer from main memory. The processing rate  $P$  can be kept constant on an FPGA, because we can adapt the gradient computation unit's microarchitecture and increase its internal parallelism to handle more values per incoming line.

## 8.2. Computing $\Phi$ on the fly

The above analysis focuses on the case when  $\Phi$  is stored in main memory, in which case quantization helps to reduce the amount of data transferred between the main memory and FPGA. In some applications,  $\Phi$  can be calculated on the fly, inside the FPGA. Also in this case, quantization can help achieve better performance. The reason why quantizing  $\Phi$  helps, even if it can be calculated on the fly, is that a quantized  $\Phi$  saves many crucial resources (e.g., multipliers) that are limited on an FPGA. These resource savings are very important in achieving a higher internal parallelism, for instance, to speed up the computation of  $\Phi \times \mathbf{x}$ . For example, it has been shown by [28] that to go from a 64-value dot product to 128-value dot product on an FPGA, it is necessary to lower the precision of one side of the dot product to 2-bits.

## 9. CPU Implementation Details

Our CPU implementation uses handwritten code in AVX2 intrinsics and supports 4-bit, 8-bit, and 32-bit precisions. We take advantage of the sparsity of the  $x$  vectors whenever possible. The bulk of the computation is accounted for by two routines: A matrix-vector multiplication which for 4-bit and 8-bit casts its computation in terms of dot-products, and a matrix times a sparse vector, which for all three datatypes casts its computation in terms of a dense scale-and-add routine.

We used OpenMP to parallelize our implementation, XORShift to generate random numbers for stochastic rounding, and the Intel math kernel library (MKL) for the 32-bit matrix-vector multiplication. Experiments were run on an Intel Xeon CPU E3-1285L v3 3.10GHz Haswell with 32GB of RAM and 25.6 GB/s bandwidth to main memory running Debian GNU/Linux 8 (jessie), kernel 3.16.43-2+deb8u3. We use the Intel icc compiler 17.0.0, Intel IPP 2017.0.0 (r52494), and Intel MKL 2017.0.0 (Build 20160801). We use the RDTSC instruction to measure the cycle count for each iteration, and reporting the median. We disabled Turbo Boost and Hyper-threading to avoid the effects of frequency scaling and resource sharing on the measurements.

## 10. Toy Example: Gaussian Data

We also investigate the performance of low precision IHT on a toy example: when data points are drawn from Gaussian distribution. Comparison of normalized IHT to other state-of-art methods is performed, for example, in [10, 11]. For Gaussian matrices, it is well known that they satisfy the restricted isometry property with high probability. Motivated by this, we apply low precision IHT to a data set where observations, entries of measurement matrix and noise are independently drawn from a zero mean and unit variance Gaussian distribution. We compute the recovery error and exact support recovery over 100 realizations of data where  $\Phi \in \mathbb{R}^{256 \times 512}$  and  $\mathbf{y}, \mathbf{e} \in \mathbb{R}^{256}$  at different SNR levels. The results are demonstrated in Fig. 11. 2&8 bit IHT performs slightly worse on Gaussian data, however is robust to noise as good as 32 bit IHT.

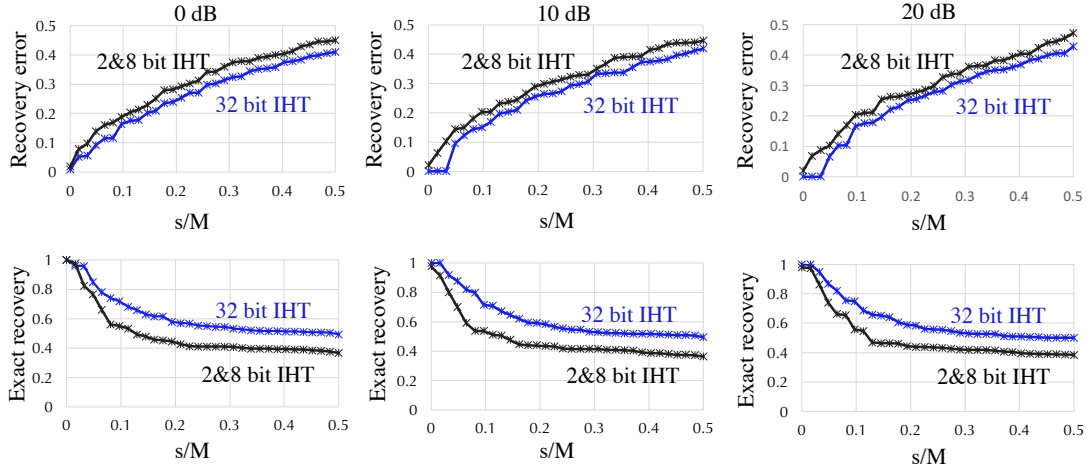


FIG 11. Comparison of 2&8 bit IHT to 32 bit IHT on Gaussian distributed data. The results are averaged over 100 realizations. Recovery error is calculated by  $\|\mathbf{x}^{[n]} - \mathbf{x}^s\|_2 / \|\mathbf{x}^s\|_2$  and exact recovery is given by the ratio between the cardinalities of recoverable support and true support.

## References

- [1] A. Ai, A. Lapanowski, Y. Plan, and R. Vershynin. One-bit compressed sensing with non-gaussian measurements. *arXiv:1208.6279*, 2012.
- [2] S.J. Wijnholds A.J. van der Veen. Signal processing tools for radio astronomy. *Handbook of Signal Processing Systems*, 2013.
- [3] D. Alistarh, J. Li, R. Tomioka, and M. Vojnovic. Qsgd: Randomized quantization for communication-optimal stochastic gradient descent. *arXiv:1610.02132*, 2016.
- [4] S. Bhatganar, T. Cornwell, T. J. Golap, and J. M. Uson. Correcting direction-dependent gains in the deconvolution of radio interferometric images. *Astronomy and Astrophysics*, 487:419–429, 2008.
- [5] J. D. Blanchard, J. Tanner, and K. Wei. Conjugate gradient iterative hard thresholding: Observed noise stability for compressed sensing. *Oxford Numerical analysis group preprint*, 2013.
- [6] T. Blumensath. Accelerated iterative hard thresholding. *The Journal of Fourier Analysis and Applications*, 92(3):265–274, 2012.
- [7] T. Blumensath. Compressed sensing with nonlinear observations and related nonlinear optimization problems. *IEEE Transactions of Information Theory*, 59(6):3466–3474, 2013.
- [8] T. Blumensath and M.E. Davies. Iterative thresholding for sparse approximations. *The Journal of Fourier Analysis and Applications*, 14(5-6):629–654, 2008.
- [9] T. Blumensath and M.E. Davies. Iterative thresholding for compressed sensing. *Applied and Computational Harmonic Analysis*, 27(3):265–274, 2009.
- [10] T. Blumensath and M.E. Davies. Normalized iterative hard thresholding: Guaranteed stability and performance. *IEEE Selected Topics in Signal Processing*, 4(2):298–309, 2010.

- [11] T. Blumensath, M.E. Davies, and G. Rilling. Greedy algorithms for compressed sensing. In Y. C. Eldar and G. Kutyniok, editors, *Compressed Sensing: Theory and Applications*, pages 348–393. Cambridge University Press., Cambridge, GB, 2012.
- [12] P. Boufounos and R. G. Baraniuk. 1-bit compressive sensing. *Conference on Information Science and Systems*, 2009.
- [13] E. Candes. The restricted isometry property and its implications for compressed sensing. *Comptes Rendus Mathematique*, 346(9-10):589–592, 2008.
- [14] E. J. Candes, J. Romberg, and T. Tao. Robust uncertainty principles: Exact signal reconstruction from highly incomplete frequency information. *IEEE Transactions of Information Theory*, 52(2):489–509, 2006.
- [15] E. J. Candes, J. Romberg, and T. Tao. Stable signal recovery from incomplete and inaccurate measurements. *Communications on pure and applied mathematics*, 59(8):1207–1223, 2006.
- [16] V. Cevher. On accelerated hard thresholding methods for sparse approximation. *Wavelets And Sparsity Xiv*, 8138, 2011.
- [17] R. Chartrand and V. Staneva. Restricted isometry properties and nonconvex compressive sensing. *Inverse Problems*, 24, 2008.
- [18] M. A. Davenport, Y. Plan, E. can den Berg, and M. Wooters. 1-bit matrix completion. *arXiv:1209.3672*, 2012.
- [19] D. L. Donoho. Compressed sensing. *IEEE Transactions of Information Theory*, 52(4):1289–1306, 2006.
- [20] Anna Gilbert and Piotr Indyk. Sparse recovery using sparse matrices. *Proceedings of the IEEE*, 98(6):937–947, 2010.
- [21] S. Gopi, P. Netrapalli, P. Jain, and A. Nori. One-bit compressed sensing: Provable support and vector recover. In *International Conference on Machine Learning*, 2013.
- [22] A. Gupta, R. Nowak, and B. Recht. Sample complexity for 1-bit compressed sensing and sparse classification. *IEEE Internation Symposium on Information Theory*, 2010.
- [23] S. Gupta, A. Agrawal, K. Gopalakrishnan, and P. Narayanan. Deep learning with limited numerical precision. In *International Conference on Machine Learning*, 2013.
- [24] J. A. Hogbom. Aperture synthesis with a non-regular distribution of interferometer baselines. *Astronomy and Astrophysics Supplement*, 15:417, 1974.
- [25] W. C. Hu and N. Kaabouch, editors. *Scalable data mining, archiving, and big data management for the next generation*. IGI Global, 2014.
- [26] I. Hubara, M. Courbariaux, D. Soudry, R. Al-Yaniv, and Y. Bengio. Quantized neural networks: Training neural networks with low precision weights and activations. *arXiv:1609.07061*, 2016.
- [27] L. Jacques, J. N. Laska, and P. Boufounos. Robust 1-bit compressive sensing via binary stable embeddings of sparse vectors. *CORR: 1104.3160*, 2012.
- [28] K. Kara, D. Alistarh, G. Alonso, O. Mutlu, and C. Zhang. Fpga-accelerated dense linear machine learning: A precision-convergence trade-off. In *Field-Programmable Custom Computing Machines (FCCM), 2017 IEEE 25th Annual International Symposium on*, pages 160–167. IEEE, 2017.
- [29] J. N. Laska, Z. Wen, W. Yin, and R. G. Baraniuk. Fast and accurate signal recovery from 1-bit compressive measurements. *IEEE Transactions on Signal Processing*, 59(11):5289–5301, 2011.

- [30] F. Li, T. J. Cornwell, and F. de Hoog. The application of compressive sampling to radio astronomy 1: Deconvolution. *Astronomy and Astrophysics Manuscript*, 15:417, 2011.
- [31] F. Li, B. Zhang, and B. Liu. Ternary weight networks. *arXiv:1605.04711*, 2016.
- [32] B. Liu, X. T. Yuan, L. Wang, Q. Liu, and D. N. Metaxas. Dual iterative hard thresholding: From non-convex sparse minimization to non-smooth concave maximization. In *International Conference on Machine Learning*, 2017.
- [33] D. Needell and J. A. Tropp. Cosamp: Iterative signal recovery from incomplete and inaccurate samples. *Applied and Computational Harmonic Analysis*, 26(3):301–321, 2008.
- [34] Y. Plan and R. Vershynin. One-bit compressed sensing by linear programming. *arXiv:1109.4299*, 2011.
- [35] Y. Plan and R. Vershynin. Robust 1-bit compressed sensing and sparse logistic regression: A convex programming approach. *CORR: 1202.1212*, 2012.
- [36] M. Rastegari, V. Ordonez, J. Redmon, and A. Farhadi. Xnor-net: Imagenet classification using binary convolutional neural networks. In *European Conference on Computer Vision*, 2016.
- [37] C. M. De Sa, C. Zhang, K. Olukotun, and C. Re. Taming the wild: A unified analysis of hogwild-style algorithms. In *Advances in Neural Information Processing Systems*, 2015.
- [38] F. Seide, H. Fu, L. G. Jasha, and D. Yu. 1-bit stochastic gradient descent and application to data-parallel distributed training of speech dnns. *Interspeech*, 2014.
- [39] G. W. Stewart. Perturbation theory for the singular value decomposition. *SVD and Signal Processing II: Algorithms, Analysis and Applications*, 1990.
- [40] G. W. Stewart. Perturbation of the svd in the presence of small singular values. *Linear Algebra and its Applications*, 2006.
- [41] G. B. Taylor, C. L. Carilli, and National Radio Astronomy Observatory R. A. Perley. Synthesis imaging in radio astronomy ii. In *ASP Conf. Series*, 1999.
- [42] R. Vaccaro. A perturbation theory for the analysis of svd-based algorithms. *IEEE International Conference on Acoustics, Speech, and Signal Processing*, 1987.
- [43] K. Wei. Fast iterative hard thresholding for compressed sensing. *IEEE Signal Processing Letters*, 22(5), 2015.
- [44] S. Wenger, S. Darabi, P. Sen, K. H. Glassmeier, and M. Magnor. Compressed sensing for aperture synthesis imaging. *International Conference on Image Processing*, 2010.
- [45] Y. Wiaux, L. Jacques, G. Puy, A. M. M. Scaife, and P. Vanderghenst. Compressed sensing imaging techniques for radio interferometry. *Monthly Notices of the Royal Astronomical Society*, 2009.
- [46] X. T. Yuan, P. Li, and T. Zhang. Gradient hard thresholding pursuit for sparsity-constrained optimization. In *International Conference on Machine Learning*, 2014.
- [47] X. T. Yuan, P. Li, and T. Zhang. Exact recovery of hard thresholding pursuit. In *Advances in Neural Information Processing Systems*, 2016.
- [48] H. Zhang, J. Li, K. Kara, D. Alistarh, J. Liu, and C. Zhang. Zipml: Training linear models with end-to-end low precision, and a little bit of deep learning. In *International Conference on Machine Learning*, pages 4035–4043, 2017.
- [49] S. Zhou, Y. Wu, Z. Ni, X. Zhou, H. Wen, and Y. Zou. Convolutional neural networks using logarithmic data representation. *arXiv:1603.01025*, 2016.
- [50] S. Zhou, Y. Wu, Z. Ni, X. Zhou, H. Wen, and Y. Zou. Dorefa-net: Training low bitwidth



convolutional neural networks with low bitwidth gradients. *arXiv:1606.06160*, 2016.